Thermokarst amplifies fluvial inorganic carbon cycling and export across watershed scales on the Peel Plateau, Canada

Scott Zolkos[1,*], Suzanne E. Tank[1], Robert G. Striegl[2], Steven V. Kokelj[3], Justin Kokoszka[3], Cristian Estop-Aragonés[4,†], David Olefeldt[4]

[1]Department of Biological Sciences, University of Alberta, Edmonton, AB, T6G 2E3 Canada
[2]United States Geological Survey, Boulder, CO, 80303 USA
[3]Northwest Territories Geological Survey, Yellowknife, NT, X1A 2L9 Canada
[4]Department of Renewable Resources, University of Alberta, Edmonton, AB, T6G 2E3 Canada
*Present address: Woodwell Climate Research Center, Falmouth, MA 02540 USA
[†]Present address: Institute of Landscape Ecology, University of Münster, Münster, 48149 Germany

Correspondence to: Scott Zolkos (sgzolkos@gmail.com)

Abstract. As climate warming and precipitation increase at high latitudes, permafrost terrains across the circumpolar north are poised for intensified geomorphic activity and sediment mobilization that are expected to persist for millennia. In previously glaciated permafrost terrain, ice-rich deposits are associated with large stores of reactive mineral substrate. Over geological timescales, chemical weathering moderates atmospheric CO_2 levels, raising the prospect that mass wasting driven by terrain consolidation following thaw (thermokarst) may enhance weathering of permafrost sediments and thus climate feedbacks. These feedbacks depend upon the mineral composition of sediments (weathering sources) and the balance between atmospheric exchange of CO_2 versus fluvial export of carbonate alkalinity ($\Sigma[HCO_3^-, CO_3^{2-}]$). Working in the fluvially-incised, ice-rich glacial deposits of the Peel Plateau, northwestern Canada, we determine the effects of retrogressive thaw slump (RTS) hillslope thermokarst activity on mineral weathering sources, CO_2 dynamics, and carbonate alkalinity export, and how these effects integrate across watershed scales (~2 to 1000 km^2). We worked along three transects in nested watersheds with varying connectivity to RTS activity: a 550 m transect along a first-order thaw stream within a large RTS; a 14 km transect along a stream which directly received inputs from several RTSs; and a 70 km transect along a larger stream with headwaters that lay outside of RTS influence. In undisturbed headwaters, stream chemistry reflected CO_2 from soil respiration processes and atmospheric exchange. Within the RTS, rapid sulfuric acid carbonate weathering, prompted by the exposure of sulfide- and carbonate-bearing tills, appeared to increase fluvial CO_2 efflux to the atmosphere and propagate carbonate alkalinity across watershed scales. Despite covering less than 1% of the landscape, RTS activity drove carbonate alkalinity to increase by two orders of magnitude along the largest transect. Amplified export of carbonate alkalinity together with isotopic signals of shifting DIC and CO_2 sources along the downstream transects highlight the dynamic nature of carbon cycling that may typify glaciated permafrost watersheds subject to intensification of hillslope thermokarst. The balance between CO_2 drawdown in regions where carbonic acid weathering predominates and CO_2 release in regions where sulfides are more prevalent will determine the biogeochemical legacy of thermokarst and enhanced weathering in northern permafrost terrains. Effects of RTSs on carbon cycling can be expected to persist for millennia and should spur their integration into predictions of weathering-carbon-climate feedbacks among thermokarst terrains.

1 Introduction

Riverine export of carbonate alkalinity ($\Sigma[HCO_3^-, CO_3^{2-}]$), generated by the chemical weathering of silicate and carbonate minerals, is a key component of the global carbon cycle and Earth's long-term climate (Berner, 1999; Gaillardet et al., 1999; Hilton and West, 2020; Torres et al., 2017). The degree to which carbonate alkalinity production involves CO_2 (as carbonic acid, $H_2CO_3 = H_2O + CO_{2(g,aq)}$), from atmospheric or soil-respiration sources, and liberates mineral carbon influences whether dissolved inorganic carbon (DIC = $\Sigma[CO_2$, carbonate alkalinity]) in fluvial networks represents a carbon sink or source. Rapid warming at northern latitudes (Serreze and Barry, 2011) is thawing permafrost (Biskaborn et al., 2019), increasing vegetation productivity (Bjorkman et al., 2018), intensifying hydrologic cycles (Rawlins et al., 2010), and strengthening land-freshwater linkages (Vonk et al., 2019; Walvoord and Kurylyk, 2016). These processes are activating large amounts of mineral substrate into biogeochemical cycles, with significant implications for DIC cycling (Lacelle et al., 2019; Wadham et al., 2019). In recent decades, increasing riverine fluxes of carbonate alkalinity and solutes across the circumpolar north reflect enhanced mineral weathering associated with active layer thickening, deepening hydrologic flowpaths into mineral soils, and greater soil acidity from increasing vegetation productivity (Drake et al., 2018a; Tank et al., 2016; Toohey et al., 2016). Glaciated permafrost terrains hosting ice-rich deposits of reactive sediments are thought to be distributed across the northern permafrost zone, raising the prospect that terrain consolidation following thaw (thermokarst) and associated carbonate alkalinity production and export may have stronger influence on climate feedbacks in such regions (Zolkos et al., 2018).

Three coupled factors primarily influence the degree to which carbonate alkalinity represents a carbon sink or source. First, the weathering source, which accounts for both the mineral composition of substrate subjected to chemical weathering and the acid(s) responsible for weathering. Silicate weathering by H_2CO_3 generates alkalinity without liberating mineral carbon and thus represents a long-term CO_2 sink. In contrast, H_2CO_3 carbonate weathering is a CO_2 sink only over ~10^2–10^3 y, as half of the alkalinity produced is geogenic. HCO_3^- produced during carbonate weathering in the presence of strong acids, for instance sulfuric acid (H_2SO_4) from sulfide oxidation, is a CO_2 source over longer timescales (~10^6 y; Calmels et al., 2007) and can also produce CO_2 over shorter timescales when H_2SO_4 is present in excess (Stumm and Morgan, 1996). Second, the rate of mineral weathering and processes that further alter this rate. Rates of chemical weathering are orders of magnitude faster for carbonates and sulfides than for silicates (Stumm and Morgan, 1996). Further, weathering rates generally increase with mineral surface area, and therefore are often fast in glacial environments owing to intense physical weathering (Anderson, 2007). Indeed, hydrochemical signatures of trace carbonate and sulfide lithologies can dominate weathering fluxes in primarily silicate glacial environments (Anderson, 2007). The disparity is so significant that, when sediment supplies are sufficient, H_2CO_3 carbonate weathering in proglacial streams can consume dissolved CO_2 to below atmospheric levels (Sharp et al., 1995; St. Pierre et al., 2019). Third, the magnitude of carbonate alkalinity export, which is influenced by its production via weathering of minerals during fluvial transport (e.g. Striegl et al., 2007) and its loss via carbonate equilibrium reactions and CO_2 degassing along the land-freshwater-ocean continuum. From a climate perspective, the magnitude of carbonate alkalinity export is particularly relevant

over geological timescales, because half of riverine carbonate alkalinity exported to the ocean is returned to the atmosphere as CO_2 via precipitation reactions within the marine carbon cycle (Calmels et al., 2007). Together, these three controls on carbonate alkalinity highlight the non-conservative nature of DIC and its susceptibility to transformation within fluvial networks. Hence, to constrain carbonate alkalinity export in rapidly changing permafrost terrains, nested-watershed sampling designs are critical for capturing DIC transformation along the land-freshwater-ocean continuum and resolving drivers and sources of carbon cycling across scales (Drake et al., 2018b).

Glaciated permafrost terrains are poised for rapid geomorphic and associated biogeochemical change as the climate warms and precipitation intensifies (Kokelj et al., 2017b). Despite glacial retreat across much of the circumpolar north, permafrost within these landscapes preserves biogeochemical legacies of glaciation across northern Canada, Alaska, and western Siberia (Kokelj et al., 2017b). In North America, the comminution of carbonate and shale bedrock during expansion of the Laurentide Ice Sheet (LIS) and the climate and vegetative protection of ice- and sediment-rich tills in the wake of its retreat endowed former glacial margins across northwestern Canada with thick inorganic tills held in ice-rich permafrost (Kokelj et al., 2017b). Today, the climate-driven renewal of post-glacial landscape change is mobilizing immense stores of minerals into modern biogeochemical cycles via hillslope thermokarst features, the largest of which include retrogressive thaw slumps (RTSs) (Kokelj et al., 2017a). On the Peel Plateau (NWT, Canada), RTSs expose carbonate- and sulfide-bearing glacigenic permafrost sediments that are tens of meters thick. The chemical weathering and fluvial transport of these sediments results in increased HCO_3^- immediately downstream of RTSs and greater solute and sediment loads throughout downstream systems (Kokelj et al., 2013; Malone et al., 2013; Zolkos et al., 2018). RTS activity has been suggested, but not previously proved, to be partly responsible for increasing carbonate alkalinity fluxes in the larger Peel River during recent decades (Zolkos et al., 2018). Yet, it remains unknown how hillslope thermokarst effects on mineral weathering and DIC sources and cycling integrate across watershed scales on the Peel Plateau and in relatively inorganic-rich permafrost terrains elsewhere. In this study we evaluated trends in major ions, DIC concentration, and dual δ^{13}C-DIC–δ^{13}C-CO_2 isotopes along transects within three nested watersheds in the Stony Creek watershed on the Peel Plateau. Our nested watershed approach was intended to allow us to determine how RTS effects on carbon cycling integrate across scales from ~1 to 1000 km^2.

2 Methods

2.1 Study Area

The Stony Creek watershed is located southwest of the hamlet of Fort McPherson, in the northern, or lower Peel River watershed (Fig. 1). Stony Creek, a tributary of the Peel River, originates in the Richardson Mountains, where slopes are sparsely vegetated and mainly consist of bedrock colluvium (Duk-Rodkin and Hughes, 1992). Exposed marine shale and sandstone bedrock contain sulfide- and gypsum-bearing lithologies, but limited carbonate (Norris, 1985). As Stony Creek flows eastward, the main channel and its tributaries incise ice-rich glacial deposits and underlying Cretaceous bedrock, forming a stream network comprised of tundra flow tracks grading to incised gravel bed streams with increasing watershed size. The fluvially-incised valleys and increasing regional precipitation have

proven conducive to thaw-driven mass wasting of ice-rich glacial deposits and formation of RTSs (Kokelj et al., 2017b). Growth of RTSs is driven by the ablation of exposed ground ice and is perpetuated by the downslope mass
110   wasting of thawed material via fluidized earth flows, which can accumulate large volumes of debris in stream valleys (Fig. 1). Across the Stony Creek watershed, intensifying RTS activity releases large volumes of sediment and solutes into streams relative to undisturbed headwaters (Kokelj et al., 2017b; Segal et al., 2016). This substrate is transported to streams via rill runoff channels in the scar zone and debris tongue deposits in the stream valley. Impacts to Stony Creek are representative of numerous other major Peel River tributaries that have incised the ice-
115   rich Peel Plateau (Kokelj et al., 2015). The ~60 km^2 watershed of Dempster Creek, a tributary of Stony Creek, originates in willow and open spruce taiga without RTS activity, receiving large inputs of sediments and solutes from RTSs FM2 and FM3 within several kilometers of the headwaters (Kokelj et al., 2013; Malone et al., 2013). Many small, non-RTS affected streams and several larger RTS-affected tributaries flow into Dempster Creek before its confluence with Stony Creek.

120   **2.2 Stream Sampling**

In late July 2017, we sampled along transects within three nested watersheds (Fig. 1, Table A1) to understand how the effects of RTSs integrate across watershed scales. (i) The *RTS FM2 runoff* transect included five sampling locations along a 550 m-long thaw stream formed by a runoff channel within an active RTS. The RTS FM2 runoff received no observable hydrologic inputs during the sampling period. (ii) A 14 km transect along the mainstem of
125   *Dempster Creek*, which received inputs directly from RTS FM2, was sampled at one location in undisturbed headwaters and at three sites downstream of RTS FM2. Sites downstream were located on the mainstem, immediately upstream of three major tributaries. We also sampled from the tributaries near their confluence with Dempster Creek, to characterize tributary chemistry. (iii) A 70 km transect along the mainstem of *Stony Creek*, a 6th-order stream, was sampled at eight locations: one in undisturbed headwaters and seven on the RTS-affected reach
130   upstream of major tributaries. We additionally sampled from one tributary of the undisturbed headwaters and from six RTS-affected tributaries near their confluence with the mainstem. Stony Creek, a major tributary of the 70000 km^2 Peel River watershed (Fig. 1), was sampled to determine how the effects of RTS activity on DIC integrate across broader scales.

At all sampling sites, stream temperature, specific conductance (henceforth, "conductivity"), and pH were measured
135   using a pre-calibrated YSI Professional-Plus water quality meter. At most sites, water samples were collected for ions, DIC, CO_2, CH_4, dissolved organic carbon (DOC), UV-visible absorbance, and total suspended solids (TSS). Along the RTS FM2 runoff transect, we sampled only for DIC and CO_2 concentration, and stable isotopes of dissolved CO_2 (δ^{13}C-CO_2). One day prior, additional parameters were sampled at RTS FM2 runoff site five, located near the confluence of the RTS runoff with Dempster Creek, for comparison with the full suite of chemistry
140   parameters collected along the Dempster Creek transect. At the Dempster and Stony Creek sites, we additionally sampled water for stable isotopes of DIC (δ^{13}C-DIC) and used dual δ^{13}C-DIC–δ^{13}C-CO_2 isotopes to characterize abiotic and biotic processes influencing DIC sources and cycling across watershed scales.

Water samples were collected from the thalweg where possible, as an integrated sample from ~15 cm below the surface to ~1 m depth. An additional sample for TSS was collected in a 1 L HDPE in the same fashion. Water samples were filtered using sample-rinsed 0.45 µm polyethersulfone (PES, ThermoFisher) or cellulose-acetate (CA, Sartorius) membranes. Samples for DIC were collected without headspace in airtight syringes. Samples for ions, DOC, and UV-visible absorbance were collected in acid washed (24 h, 10% v/v HCl) all-plastic syringes. Syringes were triple sample-rinsed, sealed without headspace, and stored cool and dark until processing within 10 h. Water for DIC was filtered (PES) into precombusted (5 h, 500°C) glass vials without headspace and sealed with a butyl rubber septum for DIC concentration or two silicone-teflon septa for δ^{13}C-DIC. Samples for cations were filtered (CA) into acid-washed bottles and acidified with trace metal-grade HNO_3, while anions were filtered (CA) but not acidified. Samples for DOC were filtered (PES) into precombusted glass vials and acidified to pH < 2 using trace metal-grade HCl (Vonk et al., 2015). Samples for UV-visible absorbance were filtered (PES) into non-acid washed 30 mL HDPE bottles. Samples were refrigerated (4°C, dark) until analysis.

Dissolved gases were collected following the headspace equilibration method (Hesslein et al., 1991) and stored in airtight syringes (for CO_2 concentration) or over-pressurized in pre-evacuated serum bottles sealed with pre-baked (60°C, 12 h), gas-inert butyl rubber stoppers (for δ^{13}C-CO_2, CH_4). At each site, atmospheric samples for CO_2 and CH_4 concentration and δ^{13}C-CO_2 were stored in the same fashion. Gas samples were stored in the dark at ~20°C prior to analysis within 10 h (CO_2) or two months (δ^{13}C-CO_2, CH_4). Water and air temperature, atmospheric pressure, and the volumetric ratio of sample to atmospheric headspace was recorded for correcting later calculations of CO_2 partial pressure (pCO$_2$) and δ^{13}C-CO_2 (Hamilton and Ostrom, 2007).

2.3 Hydrochemical Analyses

Upon returning from the field each day, CO_2 was measured using an infrared gas analyzer (PP Systems EGM-4) which was checked monthly for drift using a commercial standard (Scotty Gases). We calculated pCO$_2$ using Henry's constants corrected for stream water temperature (Weiss, 1974) and accounting for the ratio of water volume to headspace during sample equilibration. DIC samples were measured by infrared CO_2 detection (LiCOR 7000) following acidification within a DIC analyzer (Apollo SciTech model AS-C3). Calibration curves were made daily using certified reference material (CRM) from Scripps Institution of Oceanography. Samples with DIC concentrations < 400 µM were analyzed using solutions prepared from a 1000 ppm TIC stock (ACCUSPEC) that were calibrated with CRM. DIC species (CO_2, HCO_3^-, CO_3^{2-}) were calculated from DIC concentration and pCO$_2$ or pH using CO2sys (v.2.3) (Pierrot et al., 2006), using field temperature and pressure at the time of sampling, and the freshwater equilibrium constants for K1 and K2 (Millero, 1979).

Cations and trace elements were measured by optical emission spectrometry (Thermo ICAP-6300) and anions by ion chromatography (Dionex DX-600) at the University of Alberta Biogeochemical Analytical Services Laboratory (BASL, ISO/EIC accreditation #17025). DOC was measured using a total organic carbon analyzer (Shimadzu TOC-V). DOC standard curves were made daily with a 1000 ppm KHP solution (ACCUSPEC) and an in-house caffeine

standard (10 mg L^{-1}) was run every 20 samples to monitor instrument drift. Absorbance spectra were analyzed using an Ocean Optics UV-VIS instrument with a Flame spectrometer module, following Stubbins et al. (2017) and corrected for Fe interference (Poulin et al., 2014). To evaluate organic carbon reactivity, we used specific ultraviolet absorbance at 254 nm (SUVA$_{254}$) to infer DOC aromaticity (Weishaar et al., 2003).

δ^{13}C-DIC was determined using an isotope ratio mass spectrometer (Finnigan Mat DeltaPlusXP) interfaced to a total organic carbon analyzer (OI Analytical Aurora Model 1030W) at the University of Ottawa Stable Isotope Laboratory. δ^{13}C-CO$_2$ and CH$_4$ concentration were analyzed within two months using a Picarro isotope analyzer (G2201-i; < 0.2‰ precision, CH$_4$ operational range = 1.8–1500 ppm) equipped with an injection module for discrete samples (SSIM). Commercial δ^{13}C-CO$_2$ and CH$_4$ standards were used to check for drift during each run. We used mass balance to correct δ^{13}C-CO$_2$ values for the δ^{13}C and mass of atmospheric CO$_2$ used for equilibration (Hamilton and Ostrom, 2007). To assess δ^{13}C-CO$_2$ fractionation from calcite precipitation (Turner, 1982) and methanogenesis (Campeau et al., 2018) in RTS FM2 runoff, we calculated the saturation index (SI) and partial pressure of CH$_4$ (pCH$_4$). SI was calculated using the hydrochemical software Aqion version 6.7.0 (http://www.aqion.de), which uses the U.S. Geological Survey software PHREEQC (Parkhurst and Appelo, 2013) as the internal numerical solver. Samples for atmospheric and dissolved CH$_4$ were collected in the same fashion as δ^{13}C-CO$_2$. pCH$_4$ was calculated using Bunsen solubility coefficients (Wiesenburg and Guinasso, 1979) converted to the appropriate units (Sander, 2015).

TSS samples were filtered onto muffled (450˚C, 4 h) and pre-weighed glass fiber filters (Whatman GF/F; 0.7 μm nominal pore size) upon returning from the field, stored frozen, and dried (60˚C, 24 h) for gravimetric analysis following a modified version of U.S. Geological Survey Method I-3765.

2.4 Mineral Weathering and DIC Sources

We used a Piper diagram (Piper, 1944), which reflects the proportional equivalent concentrations of ions in a sample relative to mineral weathering end-members, as one method to constrain the sources of mineral weathering and HCO$_3^-$. The products of Eq. 1–7 defined the mineral weathering end-members in the Piper diagram (Table 1). We further constrained mineral weathering and DIC sources using δ^{13}C-DIC and pH. End-member δ^{13}C-DIC ranges for equilibrium processes (mixing with atmospheric and/or biotic CO$_2$) and kinetic reactions (mineral weathering) were derived following Lehn et al. (2017) and using published isotopic fractionation factors (Zhang et al., 1995).

To evaluate potential effects on δ^{13}C-CO$_2$ from DIC speciation along the pH continuum (Eq. 8, Table 1) (Clark and Fritz, 1997), we compared theoretical and observed δ^{13}C-CO$_2$ values in the Stony Creek mainstem. Theoretical δ^{13}C-CO$_2$ values were calculated using mass balance to obtain δ^{13}C-HCO$_3^-$ from measurements of DIC, CO$_2$, HCO$_3^-$, δ^{13}C-DIC, and δ^{13}C-CO$_2$. We then used measurements of stream temperature (T) to calculate the equilibrium fractionation between CO$_2$ and HCO$_3^-$ ($\varepsilon = -9.483 \times 10^3/T + 23.89$‰; Mook et al., 1974). Finally, ε was subtracted from δ^{13}C-HCO$_3^-$ to obtain theoretical δ^{13}C-CO$_2$. Similarity between observed and theoretical δ^{13}C-CO$_2$ values was

210   interpreted as $\delta^{13}C\text{-}CO_2$ variability driven by carbonate equilibrium reactions, whereas dissimilarity was taken to reflect effects from CO_2 degassing (Zhang et al., 1995) and/or biotic CO_2 production (Kendall et al., 2014).

2.5 Geospatial Analyses

Stream networks and watershed areas were delineated using the ArcHydro tools in ArcGIS 10.5 from the gridded (30 m) Canadian Digital Elevation Model (CDEM). CDEM data were reconditioned using National Hydro Network
215   stream vectors, which were first modified as needed to align with stream flow paths visible in Copernicus Sentinel-2 multispectral satellite imagery (2017; European Space Agency, https://sentinel.esa.int/). To statistically assess landscape controls on DIC cycling (Sect. 2.7), we delineated active RTSs and derived terrain roughness and vegetation productivity in the major tributary watersheds of Stony Creek. RTSs were interpreted as active where exposed sediment visibly dominated the feature surface (Cray and Pollard, 2015) in orthorectified SPOT
220   multispectral imagery that we pan-sharpened to 1.6 m resolution using the ArcGIS Image Analysis tool. The satellite imagery was collected from September 9 to 25, 2016. Active RTSs that were connected to streams were manually delineated using ArcGIS. We used RivEx 10.25 software (Hornby, 2017) to quantify the number of active RTSs impacting streams in the Stony Creek watershed and to visualize RTS impact accumulation across the fluvial network. We defined RTS impact accumulation as the cumulative number of active RTSs impacting upstream
225   reaches. RTSs were interpreted to impact streams based on contact or interpreted downslope flow based on slope direction and gradient from the CDEM (Supplementary Information). Where a single RTS affected multiple streams, only the upstream segment was used for the accumulation.

We used the Geomorphic and Gradients Metrics Toolbox (Evans et al., 2014) to calculate terrain roughness, which is a measure of variance across a land surface and represents topographic complexity (Riley et al., 1999). We use
230   terrain roughness as a proxy for potential physical erosion, which is known to enhance sulfide oxidation by exposing shale regolith throughout the Peel River watershed (Calmels et al., 2007) and may therefore influence DIC. The enhanced vegetation index (EVI) was used to broadly evaluate vegetation productivity (Huete et al., 2002), which is known to influence DIC production by enhancing mineral weathering (Berner, 1999). We used the U.S. National Aeronautics and Space Administration EVI product (Didan, 2015), which is derived from gridded (250 m) moderate
235   resolution imaging spectroradiometer (MODIS). The MODIS data were collected on July 28, 2017. The ArcGIS Zonal Statistics tool was used to calculate total RTS area, mean terrain roughness, and mean EVI in Stony Creek tributary watersheds.

2.6 Stream Flow

Water discharge (Q) in Stony Creek tributaries was estimated from a hydraulic geometry model (Gordon et al.,
240   2004) that we developed using flow measurements made in Peel Plateau streams during 2015–2017 and width (W) estimated from on-site measurements or photos from 2017 with a known scale. The model reflected measurements spanning diverse stream morphologies ($W = 0.4$–6.6 m) and flow conditions ($Q = 0.005$–0.91 m^3 s^{-1}) (Fig. A1):

$$Q = e^{\ln(W / 6.258) / 0.661} \; (p < 0.001, R^2 = 0.89, F_{1,18} = 150) \quad (1)$$

Discharge values from 2015 to 2017 were calculated from measurements of stream flow (RedBack Model RB1, PVD100) and cross-sectional area made at increments equal to 10% of stream width (Gordon et al., 2004; Lurry and Kolbe, 2000), and were averaged for sites with multiple measurements.

2.7 Statistics

We tested for downstream change in HCO_3^- concentration and pCO_2 along the Stony Creek mainstem using the non-parametric Mann-Kendall test from the R software (R Core Team, 2018) package *zyp* (Bronaugh and Werner, 2013), following the trend pre-whitening approach detailed by Yue et al. (2002) to account for serial autocorrelation. We developed a multiple linear regression model to evaluate the influence of RTS activity on HCO_3^- export in Stony Creek tributary watersheds relative to other landscape variables known to influence DIC production, including hydrology, terrain roughness, and vegetation productivity (Berner, 1992; Drake et al., 2018a). To account for potential effects of varying tributary watershed areas on discharge (Q) and constituent concentration, we used tributary HCO_3^- yields in the model. Instantaneous discharge (Q, m^3 s^{-1}) was estimated from the hydraulic geometry relationship between Q and stream width (Eq. 1). Discharge and HCO_3^- flux (concentration*Q) were normalized to the respective tributary watershed area and scaled to estimate daily water yield (cm d^{-1}) and HCO_3^- yield (μmol m^{-2} d^{-1}). Daily HCO_3^- yields in Stony Creek tributaries were modeled as:

$$HCO_3^- \; yield = RTS_n + RTS_{area} + Water \; yield + TR + EVI \quad (2)$$

where RTS_n is the number of active RTSs; RTS_{area} is the watershed area disturbed by RTSs (%); TR is the mean terrain roughness (m); and EVI is the mean enhanced vegetation index (–1 to 1). The multiple linear regression was trimmed using the *step* function in the R package *lmerTest* (Kuznetsova et al., 2018) to eliminate covariates which did not improve the model. Highly collinear covariates were identified using a Variance Inflation Factor > 3 (Zuur et al., 2010) and removed from the trimmed models. Model fits were inspected visually with residual plots and covariates were transformed as needed to meet assumptions of independent and homoscedastic residuals (Zuur, 2009). To understand potential effects from variable rainfall on water yields prior to and during the two-day sampling window of the Stony Creek tributaries, we inspected total rainfall in 24 h increments preceding the sampling of each Stony Creek tributary. Hourly rainfall data were obtained from a Government of Northwest Territories Total meteorological station located ~1 km from the RTS FM2 (Fig. A2). Statistics were performed in the R programming environment (v.3.4; R Core Team, 2018) and significance was interpreted at $\alpha = 0.05$. Summary statistics are reported as mean ± standard error, unless noted.

3 Results

3.1 pH, Ions, and Weathering Sources Across Watershed Scales

Geochemistry of the mainstem and tributary sites are summarized in Table 2. Among sites, pH was generally circumneutral and conductivity was higher in proximity to RTS activity. pH was highest in the RTS FM2 runoff (7.69 ± 0.05, mean $\pm$ SE), intermediate in Dempster Creek (7.07 ± 0.42), and lowest in Stony Creek (6.86 ± 0.21). Along the RTS FM2 runoff transect, pH decreased from 7.72 to 7.51 between sites one and two, and increased thereafter to 7.80 at site five. pH in the Dempster Creek headwaters (5.82) was lower than in the RTS-affected reach (7.48 ± 0.1). In Stony Creek pH, increased from 5.66 in headwaters to ~7.30 at sites 6–8.

Similar to pH, conductivity was higher in the RTS FM2 runoff ($1799 \pm 111 \; \mu S \; cm^{-1}$) than in Dempster Creek (520 ± 191) and Stony Creek (320 ± 19). Conductivity in RTS FM2 increased from 1370 to $1990 \; \mu S \; cm^{-1}$. Along Dempster Creek, conductivity increased from $52 \; \mu S \; cm^{-1}$ in the undisturbed headwaters to $958 \; \mu S \; cm^{-1}$ at the first site downstream of RTS FM2, and decreased downstream thereafter. In Stony Creek, conductivity decreased between the headwaters and the fourth downstream site, and was relatively constant at ~$285 \; \mu S \; cm^{-1}$ along the lower reach of Stony Creek (sites 5–8).

Streams were characterized by Ca^{2+}–Mg^{2+}–SO_4^{2-}-type waters (Fig. 2) with low concentrations of Cl^- relative to SO_4^{2-}, reflecting a predominance of H_2SO_4 carbonate weathering and sulfate salt (e.g. gypsum) dissolution over other mineral weathering sources. A relatively greater proportion of SO_4^{2-} than HCO_3^- in the RTS FM2 runoff and along the upper reach of Stony Creek (sites 1–4) (Fig. 2a) suggests greater sulfate salt dissolution and/or that carbonate weathering at these sites buffered less H_2SO_4 (Eq. 7) than in Dempster Creek headwaters and its tributaries (Eq. 3). Along the Stony Creek mainstem (sites 1–8), increasing HCO_3^- (Fig. 2a) reflected inputs from RTS-affected tributaries (sites 2–7) having relatively more HCO_3^--type waters (Fig. 2b) from H_2SO_4 and potentially H_2CO_3 carbonate weathering.

3.2 HCO_3^- Concentration and pCO₂

Carbonate alkalinity ($HCO_3^- + CO_3^{2-}$) was primarily HCO_3^- (>99%) at all sites. HCO_3^- was highest in the RTS FM2 runoff ($1429 \pm 23 \; \mu M$), intermediate in Dempster Creek ($864 \pm 261 \; \mu M$), and lowest in Stony Creek ($255 \pm 59 \; \mu M$). Along the RTS FM2 runoff transect, HCO_3^- decreased from 1510 to $1386 \; \mu M$. In Dempster Creek and Stony Creek, HCO_3^- concentrations were relatively low in undisturbed headwaters (115 and $33 \; \mu M$, respectively) and two to ten times higher at the first RTS-affected site (1321 and $69 \; \mu M$, respectively). HCO_3^- decreased along the entire RTS-affected reach of Dempster Creek (from 1321 to $946 \; \mu M$) in conjunction with inputs from dozens of tributary watersheds without active RTSs. In contrast, HCO_3^- increased significantly along Stony Creek ($p < 0.01$, Mann-Kendall test) (Fig. 3a) in conjunction with inputs from RTS-affected tributaries.

CO₂ was oversaturated at all sites (Fig. 3b) and a minor component of DIC (<10%) at most sites except the undisturbed headwaters of Dempster Creek (site 1) and upper Stony Creek (sites 1–3). pCO₂ was highest in the Dempster Creek headwaters (2467 µatm), relatively high in the RTS FM2 runoff (1023 ± 137 µatm), and consistently near atmospheric levels along Stony Creek (479 ± 12 µatm). Along the RTS FM2 runoff transect, pCO₂ increased from 1046 to 1534 µatm within the first 220 m and then decreased from 1534 to 742 µatm over the final

330 m. Along Dempster Creek, pCO$_2$ decreased from 2467 in the headwaters to 686 µatm at the first RTS-affected site, and further decreased to 600 µatm by the end of Dempster Creek. pCO$_2$ in Dempster and Stony Creek tributaries were generally similar to the mainstem sites.

3.3 DOC Concentration and SUVA$_{254}$

DOC concentrations were highest in Dempster Creek (933 ± 83 µM), intermediate in the RTS FM2 runoff (758 ± 152 µM), and lowest in Stony Creek (303 ± 54 µM). Along the Dempster Creek transect, DOC decreased between the undisturbed headwaters (960 µM) and the first RTS-affected site (790 µM) and increased thereafter along the transect (to 1156 µM) (Fig. 3c). Along Stony Creek, DOC increased significantly (from 102 to 551 µM) ($p < 0.001$, Mann-Kendall test).

SUVA$_{254}$ values were lowest in the RTS FM2 runoff (1.85 ± 0.4 L mgC^{-1} m^{-1}), highest in Dempster Creek (3.10 ± 0.2 L mgC^{-1} m^{-1}), and intermediate in Stony Creek (2.51 ± 0.3 L mgC^{-1} m^{-1}). SUVA$_{254}$ values along the Dempster Creek transect followed a similar pattern to DOC and along Stony Creek SUVA$_{254}$ values doubled (Fig. 3d). DOC and SUVA$_{254}$ increased in consecutive downstream tributaries of Stony Creek, but not Dempster Creek.

3.4 Stable Isotopic Composition of Carbon in DIC and CO$_2$

δ^{13}C-DIC values were highest in the RTS FM2 runoff (–1.0‰) and lower, on average, along the mainstem Dempster Creek (–7.5 ± 2.5‰) and Stony Creek (–8.4 ± 0.5‰). In the undisturbed headwaters of Dempster and Stony Creek, relatively negative δ^{13}C-DIC values (–11.6 to –15.6‰) reflected DIC sourced from a combination of atmospheric and biogenic (soil) CO$_2$ (Fig. 4). In the RTS FM2 runoff, relatively ^{13}C-enriched δ^{13}C-DIC (–1.0‰) aligned with H$_2$SO$_4$ carbonate weathering. δ^{13}C-DIC decreased from –4.2‰ at the first site downstream of the RTS FM2 runoff to –5.7‰ at the end of Dempster Creek. Along Stony Creek, δ^{13}C-DIC increased from the undisturbed headwaters (–11.6‰) to the most downstream site (–7.8‰). δ^{13}C-DIC signals of H$_2$SO$_4$ carbonate weathering diminished slightly downstream along the Dempster Creek transect and intensified along Stony Creek (Fig. 4).

Similar to δ^{13}C-DIC, δ^{13}C-CO$_2$ values were higher in the RTS FM2 runoff (–11.0 ± 0.4‰) than along the mainstem Dempster Creek (–17.9 ± 1.4‰) and Stony Creek (–16.7 ± 0.6‰) (Fig. 5). δ^{13}C-CO$_2$ values were relatively low in the undisturbed headwaters of Dempster Creek (–21.6‰), and intermediate in the headwaters of Stony Creek (–13.8‰) (Fig. 5). Along the RTS FM2 runoff transect, δ^{13}C-CO$_2$ values increased from sites one to four (–12.1 to –10.0‰) and decreased at site five (–11.2‰). Along the RTS-affected reach of Dempster Creek, δ^{13}C-CO$_2$ values decreased from –16.0 to –18.5‰ in conjunction with inputs from non RTS-affected tributaries having relatively low δ^{13}C-CO$_2$ (–18.7 ± 1.4‰) that was more similar values from soil-respired CO$_2$. Along Stony Creek, δ^{13}C-CO$_2$ values decreased from –13.8 to –18.1‰, showing a trend opposite that of δ^{13}C-DIC (Fig. 5). Among sites, atmospheric δ^{13}C-CO$_2$ values were relatively consistent (–9.5 ± 0.4‰, mean ± SD).

Variance in $\delta^{13}C$ of CO_2 and DIC could be influenced by biotic production, CO_2 conversion to HCO_3^-, and/or
340   mixing with atmospheric CO_2. To evaluate the relative influence of these processes, we compared measured $\delta^{13}C$-CO_2 for Stony Creek with theoretical values reflecting DIC controlled by speciation along the pH continuum (Sect. 2.4). In the undisturbed headwaters, $\delta^{13}C$-CO_2 indicated stronger influence from atmospheric CO_2 (Fig. 6). Along the upper, RTS-affected reach of Stony Creek (sites 2–5, from ~5 to 35 km), the good agreement between measured and theoretical $\delta^{13}C$-CO_2 values reflected equilibrium fractionation ($\varepsilon = 9.7‰$ at 9°C) (Mook et al., 1974) between

345   CO_2 and HCO_3^-, indicating greater influence from DIC speciation (Fig. 6). Along the lower RTS-affected reach of the transect (sites 6–8), $\delta^{13}C$-CO_2 values more strongly reflected biotic CO_2 production with potential effects from degassing and/or CO_2 conversion to HCO_3^-. These trends in $\delta^{13}C$-CO_2 values along Stony Creek show a downstream change in the processes influencing DIC source, which may be related to inputs of weathering solutes and organic matter from RTS-affected tributaries.

350   **3.5 Stony Creek Tributary Carbonate Alkalinity Yields and Watershed Characteristics**

Carbonate alkalinity yields in RTS-affected tributaries of Stony Creek (1558 ± 1135 µmol m^{-2} d^{-1}, mean $\pm$ SD) were three orders of magnitude higher than in the non-RTS affected headwaters (1.8 µmol m^{-2} d^{-1}) (Table 3). Consecutive downstream tributary watersheds exhibited no clear trends in the number of RTSs, the area disturbed by RTSs, terrain roughness, or EVI. In the Stony Creek headwater tributary, which had no active RTSs, terrain roughness

355   (16.2 m) and vegetation productivity (EVI = 0.28) were higher than in the other six tributary watersheds (4.3 ± 1.3 m and 0.46 ± 0.01, mean $\pm$ SD, respectively). In the other tributary watersheds, the number of active RTSs reached 50 (15 ± 17, mean $\pm$ SD) and RTS disturbance area reached 3.5% ($0.91 \pm 1.29\%$, mean $\pm$ SD) (Table 3).

To elucidate landscape controls on carbonate alkalinity export in Stony Creek tributary watersheds, we paired geospatial data for active RTSs, terrain roughness, and vegetation productivity with estimates of carbonate alkalinity

360   and water yields in a multiple linear regression model (Sect. 2.7). Water yield and the area of RTS disturbance were retained during automated covariate selection for the final model ($F_{2,4} = 63$, $p < 0.001$, $R^2 = 0.95$). In addition to the expected relationship between water yield and carbonate alkalinity yield, RTS disturbance area was a clear, significant predictor of carbonate alkalinity yield and formed a stronger relationship with alkalinity than did water yield (Table 3).

365   **4 Discussion**

4.1 Rapid Carbon Cycling in Fluvial Network Headwaters

Within undisturbed headwaters and RTS runoff on the Peel Plateau, rapid carbon cycling enhanced fluvial CO_2 efflux to the atmosphere. In undisturbed headwaters, $\delta^{13}C$-CO_2 values indicate inputs of primarily biogenic CO_2 from soil respiration into Dempster Creek. In the Stony Creek headwaters, we also found an influence from

370   exchange with atmospheric CO_2. In the undisturbed Dempster Creek headwaters, a 70% decrease in pCO_2 within

several kilometers downstream likely reflected degassing and diminishing inputs of respired CO_2 from soils to streams, relative to headwaters (Hutchins et al., 2019). These trends resemble headwater streams elsewhere, in that hydrologic inputs of respired CO_2 from riparian soils can drive CO_2 supersaturation in fluvial network headwaters (Campeau et al., 2018; Crawford et al., 2013), which is rapidly effluxed to the atmosphere over short distances downstream (Hotchkiss et al., 2015). In contrast, trends in hydrochemistry and stable isotopes within RTS FM2 runoff demonstrate that drivers of carbon cycling within RTSs are starkly different from those in undisturbed headwaters on the Peel Plateau.

Along the RTS FM2 runoff transect, the increase in conductivity corroborates experimental evidence (Zolkos and Tank, 2020) that permafrost sediments on the Peel Plateau can rapidly weather during fluvial transport within runoff. In the upper reach of the runoff transect, near RTS FM2, the decrease in HCO_3^-, increase in CO_2, and relatively enriched $\delta^{13}C$-CO_2 (Fig. 5) indicate rapid production of geogenic CO_2 via H_2SO_4 carbonate weathering (Eq. 7) and carbonate equilibrium reactions (Eq. 8). In Yedoma terrains in Siberia and Alaska, where mineral soils are relatively more organic-rich, thermokarst is associated with rapid production of biogenic CO_2 (Drake et al., 2018b). While respiration likely produced some CO_2 in RTS FM2 runoff (Littlefair et al., 2017), observed $\delta^{13}C$-CO_2 (−11‰) more strongly reflected H_2SO_4 weathering of regional carbonate bedrock (−0.7 to −5.6‰) (Hitchon and Krouse, 1972) when accounting for isotopic fractionation of ~8‰ between carbonate and CO_2 at the temperature of FM2 runoff (18˚C) (Clark and Fritz, 1997). Along the lower reach of the FM2 runoff transect, the increase in $\delta^{13}C$-CO_2 aligned with the preferential loss of ^{12}C in the CO_2 phase via DIC fractionation and degassing (Doctor et al., 2008; Drake et al., 2018b; Kendall et al., 2014). ^{13}C enrichment of the CO_2 pool by methanogenesis (Campeau et al., 2018), photosynthesis (Descolas-Gros and Fontungne, 1990), and/or calcite precipitation (Turner, 1982) was unlikely, as CH_4 in FM2 runoff was relatively low ($pCH_4 = 3.6 \pm 1.9$ µatm, mean $\pm$ SD, $n = 6$), the high turbidity of FM2 runoff likely inhibited photosynthesis (Levenstein et al., 2018), and calcite was below saturation (SI = −0.79). These trends demonstrate that weathering of sediments during fluvial transport within RTS runoff can result in rapid CO_2 production and efflux to the atmosphere, in agreement with recent estimates of high rates of CO_2 efflux within RTS runoff (Zolkos et al., 2019).

High rates of weathering within RTS FM2 runoff aligns with observations of rapid solute production via the exposure and weathering of carbonate flour in glacial foreground environments (Anderson, 2007; Sharp et al., 1995; St. Pierre et al., 2019). Because minerals exposed by deeper RTSs are generally reactive, and sediment concentrations increased by three orders of magnitude between the undisturbed Dempster Creek headwaters and the first RTS-affected site, we reasoned that H_2CO_3 weathering of these sediments during fluvial transport would measurably influence pCO_2 along Dempster Creek (Eq. 1) (St. Pierre et al., 2019; Striegl et al., 2007). Although pCO_2 decreased along the RTS-affected reach of the Dempster Creek transect (sites 2–4, Fig. 2b), coincident decreases in conductivity, HCO_3^-, and pH (Table 2, Figs. 2a, 4) suggest that degassing and dilution associated with inputs from non RTS-affected tributaries had stronger effects on pCO_2 than did H_2CO_3 carbonate weathering, even at the relatively short scale of this 14 km transect. From a carbon cycling perspective, biogeochemically reactive

mineral substrate appears to be rapidly transformed in headwaters on the Peel Plateau; geogenic CO_2 production is relegated to within RTSs; and more stable weathering products, including alkalinity, are exported downstream.

4.2 RTS Activity in Headwaters Amplifies Carbonate Alkalinity Production and Accumulation Across Scales

Similar to CO_2, alkalinity production on the Peel Plateau was strongly coupled to primarily H_2SO_4 carbonate weathering mediated by RTS activity. This was reflected by a modest decrease in HCO_3^- along Dempster Creek in tandem with decreasing RTS disturbance area (from 3.2 to 1.2%) and some dilution by inputs from non RTS-affected tributaries. Multiple linear regression results further indicated that RTS activity was a primary terrain control on carbonate alkalinity yields. In the Stony Creek headwaters, low carbonate alkalinity yield relative to water yield suggested that HCO_3^- export was limited by carbonate availability rather than by water. In RTS-affected tributaries, higher carbonate alkalinity yields relative to water yields aligned with the model results indicating that RTS activity increases carbonate weathering and alkalinity export beyond what would otherwise be expected on the Peel Plateau. HCO_3^- yields in RTS-affected tributaries were comparable to summertime HCO_3^- yields in watersheds with carbonate rock weathering by glacial activity (~3000 $\mu mol\ m^{-2}\ d^{-1}$) (Lafrenière and Sharp, 2004; Striegl et al., 2007), emphasizing that unmodified sulfide- and carbonate-bearing sediments in regional permafrost are highly reactive (Zolkos and Tank, 2020) and primary sources of DIC within intermediate-sized (1000 km^2) fluvial networks. This aligns with stable sulfur isotopes in RTS runoff and near the Stony Creek outflow that strongly reflected sulfide oxidation (Zolkos et al., 2018). Unlike CO_2, the increase in HCO_3^- by orders of magnitude along Stony Creek in association with inputs from RTS-affected tributaries shows that more chemically stable (i.e. non-gaseous) weathering products accumulated across scales. This aligns with previous findings that solutes and sediments from RTSs propagate through fluvial networks (Kokelj et al., 2013; Malone et al., 2013), and suggests that future intensification of RTS activity (Segal et al., 2016) will increase HCO_3^- export to downstream environments.

4.3 Integration of RTS Effects on Carbon Cycling Across Watershed Scales

These findings enable us to develop a conceptual model of catchment chemical characteristics and how the effects of RTS activity on carbon cycling integrate across watershed scales on the Peel Plateau (Fig. 7). This model may be generalized to permafrost terrains elsewhere for testing hypotheses related to thermokarst effects on carbon cycling across the land-freshwater-ocean continuum (Tank et al., 2020).

In undisturbed headwaters on the Peel Plateau, DIC was primarily CO_2 and sources of CO_2 varied from relatively more atmospheric in the sparsely-vegetated and mountainous Stony Creek headwaters (Fig. 7a i), to more biogenic in the tundra-taiga headwaters of Dempster Creek (Fig. 7a ii). Downstream, CO_2 loss and mixing of streams resulted in undisturbed headwaters having relatively modest DIC comprised of a relatively large proportion of CO_2 sourced from mixing with the atmosphere and likely some inputs from soil respiration (Fig. 7a iii). Underlying the trends in CO_2 concentration, measurements of $\delta^{13}C\text{-}CO_2$ revealed shifting sources of CO_2 across scales (discussed below).

Thaw and exposure of reactive tills (Lacelle et al., 2019; Zolkos and Tank, 2020) by RTS activity in Peel Plateau

440 headwaters (see also Kokelj et al., 2013; Malone et al., 2013) promotes mineral weathering, rapidly generating CO_2 and substantial alkalinity. Alkalinity, along with large amounts of sediment (van der Sluijs et al., 2018) and organic matter (Shakil et al., 2020), are exported from RTSs into fluvial networks (Fig. 7a iv). Similar to other locations, DOC in RTS runoff on the Peel Plateau is known to be relatively biolabile (Littlefair et al., 2017), suggesting inputs from RTS FM2 to larger streams (e.g. Dempster Creek) could stimulate biotic CO_2 production.

445 CO_2 degassing is most pronounced within RTSs and in undisturbed headwaters that are strongly coupled with soil respiration, and active mineral weathering is less pronounced in mid-order streams (e.g. Dempster Creek). Hence, mid-order streams, which also mix with inputs from undisturbed tributaries, export HCO_3^- downstream at a magnitude coupled to the area of RTS disturbance (Fig. 7a v). Further, immediately downstream of the RTS FM2 inflow to Dempster Creek, the decrease in CO_2 and shift in $\delta^{13}C$-CO_2 away from a biotic source suggest that CO_2

450 degassing to the atmosphere was more prominent than respiration of permafrost DOC (Doctor et al., 2008; Drake et al., 2018b; Kendall et al., 2014). Thus, immediately downstream of RTSs, microbial respiration of permafrost DOC does not appear to generate substantial CO_2. This may be due to lower rates of DOC mineralization than degassing, and/or the protection of DOC from microbial oxidation via adsorption to RTS sediments (Gentsch et al., 2015). The latter aligns with the observed decrease in DOC concentration and increase in TSS (to 11800 mg L^{-1}) between

455 Dempster Creek sites one and two (Table 2, Fig. 3c) (see also Littlefair et al., 2017). However, these effects may diminish farther downstream in mid-order streams. Along the lower reach of Dempster Creek (sites 3–4), the decrease in $\delta^{13}C$-CO_2, increase in DOC, and $SUVA_{254}$ resembling terrestrial-origin DOC from tributary streams suggest that undisturbed tributary streams may deliver biogenic CO_2 and/or stimulate organic matter respiration in RTS-affected streams. Thus, effects of RTS sediments on CO_2 are attenuated downstream as DOC inputs increase.

460 Up to and likely beyond scales of ~10^3 km^2 (e.g. Stony Creek), the largest scale of this study, HCO_3^- concentrations are likely to increase significantly downstream, reflecting the export of relatively stable weathering products (see also Kokelj et al., 2013; Malone et al., 2013; Zolkos et al., 2018) and accumulation of carbonate alkalinity (Fig. 7a vi, Fig. 7b). These effects were primarily driven by inputs of HCO_3^- from RTS-affected tributaries, which also increased DOC significantly along Stony Creek. Potentially owing to organic matter limitation, CO_2 in the

465 undisturbed headwaters of Stony Creek appeared to be driven by relatively faster carbonate equilibrium reactions (Eq. 8) (Stumm and Morgan, 1996). In contrast, along the lower RTS-affected reach of Stony Creek, as HCO_3^- and DOC increased and pH stabilized, $\delta^{13}C$-CO_2 measurements suggest that respiration of organic matter from RTS-affected tributaries contributed to CO_2 oversaturation (Fig. 6). In higher-orders streams within RTS-affected fluvial networks, biotic CO_2 production may increase together with HCO_3^- concentrations. This trend was not evident in

470 $\delta^{13}C$-DIC, which primarily reflected inputs of geogenic DIC from RTS-affected tributaries. Thus, sources of CO_2 may shift across scales in RTS-affected fluvial networks, and measurements of $\delta^{13}C$-CO_2 highlight a decoupling between the drivers of CO_2 and HCO_3^- at larger scales (Horgby et al., 2019; Hutchins et al., 2020). A stronger signal of biogenic CO_2 production in larger streams than in permafrost thaw streams, as we observed, is opposite common trends in Yedoma terrains (Drake et al., 2018b) and may partly reflect limitation of organic substrate in Stony Creek

headwaters that is relieved by RTS inputs farther downstream (Shakil et al., 2020). Underlying these trends, RTS disturbance area increased along the Stony Creek transect, from 0% in the undisturbed headwaters to 0.36% in the tributary watersheds (sites 4–8). Despite RTS activity occupying a small proportion of the landscape, carbonate alkalinity propagated through fluvial networks. These findings directly link intensifying RTS activity on the Peel Plateau (Segal et al., 2016) with signals of increasing weathering and carbonate alkalinity export in the broader Peel and Mackenzie River watersheds (Tank et al., 2016; Zolkos et al., 2018).

4.4 Implications for Carbon Cycling in Northern Permafrost Regions

Permafrost terrains susceptible to hillslope thermokarst like RTSs occur within and outside of former glacial limits across the circumpolar north (Olefeldt et al., 2016; Zolkos et al., 2018), but variability in geology, glacial activity, climate, and ecosystem history cause permafrost mineral composition to vary between regions. The degree to which carbonate weathering is coupled with sulfide oxidation will determine if mineral weathering is a CO_2 sink (Eq. 1) or source (Eqs. 3,7) over the coming millennia (Zolkos et al., 2018). Where thermokarst releases inorganic substrate with limited prior modification – as in deeper RTSs on the Peel Plateau (Lacelle et al., 2019; Zolkos and Tank, 2020) – carbon cycling can be expected to be rapid and driven by inorganic processes, and strengthen abiotic components of the permafrost carbon-climate feedback (Schuur et al., 2015). Current dynamic-numerical biogeochemical models for the Mackenzie River basin suggest the ubiquity of sulfide minerals reduces weathering consumption of atmospheric CO_2 by half (Beaulieu et al., 2012). These models do not account for enhanced H_2SO_4 carbonate weathering associated with RTS activity, which our results show is significantly and positively correlated with alkalinity production and export across watershed scales. Further, climate feedbacks associated with RTS activity appear to be scale-dependent. RTSs rapidly generate CO_2, but its outgassing occurs mostly within runoff and comprises a small proportion of watershed-scale fluvial CO_2 efflux (Zolkos et al., 2019). Carbonate alkalinity generated within RTSs represents a much larger positive feedback to climate change, albeit over geological timescales, via carbonate precipitation reactions within the marine carbon cycle (Calmels et al., 2007). Future intensification of RTS activity (Segal et al., 2016) can thus be expected to increase geogenic CO_2 production within headwaters (see also Zolkos et al., 2019) and carbonate alkalinity export across scales (Fig. 7b) (Tank et al., 2016). Cross-scale watershed investigations will help to understand these effects across terrains with varying lithologies and permafrost composition, and the implications of hillslope thermokarst for climate feedbacks.

5 Conclusions

Climate-driven renewal of deglaciation-stage geomorphic activity and associated carbonate weathering in the western Canadian Arctic is amplifying aquatic carbon export across scales, despite RTSs disturbing only a fractional proportion of the landscape. Primary consequences include geogenic CO_2 production that is rapid, and localized to RTSs, and augments soil-respired CO_2 efflux from undisturbed headwater streams. Significant carbonate alkalinity production within and export from RTSs project through fluvial networks and likely to Arctic coastal marine environments, forecasting stronger land-freshwater-ocean linkages (Tank et al., 2016) as RTS activity intensifies in

glacial margin landscapes across northwestern Canada (Kokelj et al., 2017a). Legacy effects of RTSs on carbon

510   cycling can be expected to persist for millennia and should spur the integration of dynamic-numerical

biogeochemical models (Beaulieu et al., 2012) into predictions of weathering-carbon-climate feedbacks (Zolkos et

al., 2018) among northern thermokarst terrains (Turetsky et al., 2020).

Data availability. All data used in this study are available in the supplement.

Supplement. The supplement for this article is available online.

515   *Author contributions*. SZ and SET designed the study with contribution from RGS and SVK. SZ led the field

research, laboratory analyses, and manuscript writing. JK contributed to geospatial analyses. CEA contributed to

laboratory analyses. All authors (SZ, SET, RGS, SVK, JK, CEA, DO) contributed to manuscript writing.

Competing interests. The authors declare no conflicts of interest.

Acknowledgements. Research was supported by the Natural Sciences and Engineering Research Council of Canada,

520   Campus Alberta Innovates Program, Natural Resources Canada Polar Continental Shelf Program, Environment

Canada Science Youth Horizons, UAlberta Northern Research Award, and Arctic Institute of North America Grant-

in-Aid. We thank Rosemin Nathoo, Christine Firth, Dempster Collin, Abraham Snowshoe, Sarah Shakil, and Erin

MacDonald for assistance in the field. NWT Geological Survey contribution #. Any use of trade, product or firm

names in this publication is for descriptive purposes only and does not imply endorsement by the U.S. Government.

525   **References**

Anderson, S. P.: Biogeochemistry of Glacial Landscape Systems, Annual Review of Earth and Planetary Sciences, 35(1), 375–399, doi:10.1146/annurev.earth.35.031306.140033, 2007.

Beaulieu, E., Goddéris, Y., Donnadieu, Y., Labat, D. and Roelandt, C.: High sensitivity of the continental-weathering carbon dioxide sink to future climate change, Nature Climate Change, 2(5), 346–349,
530   doi:10.1038/nclimate1419, 2012.

Berner, R. A.: Weathering, plants, and the long-term carbon cycle, Geochimica et Cosmochimica Acta, 56(8), 3225–3231, 1992.

Berner, R. A.: A new look at the long-term carbon cycle, GSA Today, 9(11), 1–6, 1999.

Biskaborn, B. K., Smith, S. L., Noetzli, J., Matthes, H., Vieira, G., Streletskiy, D. A., Schoeneich, P., Romanovsky,
535   V. E., Lewkowicz, A. G., Abramov, A., Allard, M., Boike, J., Cable, W. L., Christiansen, H. H., Delaloye, R., Diekmann, B., Drozdov, D., Etzelmüller, B., Grosse, G., Guglielmin, M., Ingeman-Nielsen, T., Isaksen, K., Ishikawa, M., Johansson, M., Johannsson, H., Joo, A., Kaverin, D., Kholodov, A., Konstantinov, P., Kröger, T., Lambiel, C., Lanckman, J.-P., Luo, D., Malkova, G., Meiklejohn, I., Moskalenko, N., Oliva, M., Phillips, M., Ramos, M., Sannel, A. B. K., Sergeev, D., Seybold, C., Skryabin, P., Vasiliev, A., Wu, Q., Yoshikawa, K.,
540   Zheleznyak, M. and Lantuit, H.: Permafrost is warming at a global scale, Nature Communications, 10(1), doi:10.1038/s41467-018-08240-4, 2019.

Bjorkman, A. D., Myers-Smith, I. H., Elmendorf, S. C., Normand, S., Rüger, N., Beck, P. S. A., Blach-Overgaard, A., Blok, D., Cornelissen, J. H. C., Forbes, B. C., Georges, D., Goetz, S. J., Guay, K. C., Henry, G. H. R., HilleRisLambers, J., Hollister, R. D., Karger, D. N., Kattge, J., Manning, P., Prevéy, J. S., Rixen, C., Schaepman-Strub, G., Thomas, H. J. D., Vellend, M., Wilmking, M., Wipf, S., Carbognani, M., Hermanutz, L., Lévesque, E., Molau, U., Petraglia, A., Soudzilovskaia, N. A., Spasojevic, M. J., Tomaselli, M., Vowles, T., Alatalo, J. M., Alexander, H. D., Anadon-Rosell, A., Angers-Blondin, S., Beest, M. te, Berner, L., Björk, R. G., Buchwal, A., Buras, A., Christie, K., Cooper, E. J., Dullinger, S., Elberling, B., Eskelinen, A., Frei, E. R., Grau, O., Grogan, P., Hallinger, M., Harper, K. A., Heijmans, M. M. P. D., Hudson, J., Hülber, K., Iturrate-Garcia, M., Iversen, C. M., Jaroszynska, F., Johnstone, J. F., Jørgensen, R. H., Kaarlejärvi, E., Klady, R., Kuleza, S., Kulonen, A., Lamarque, L. J., Lantz, T., Little, C. J., Speed, J. D. M., Michelsen, A., Milbau, A., Nabe-Nielsen, J., Nielsen, S. S., Ninot, J. M., Oberbauer, S. F., Olofsson, J., Onipchenko, V. G., Rumpf, S. B., Semenchuk, P., Shetti, R., Collier, L. S., Street, L. E., Suding, K. N., Tape, K. D., Trant, A., Treier, U. A., Tremblay, J.-P., Tremblay, M., Venn, S., Weijers, S., Zamin, T., Boulanger-Lapointe, N., Gould, W. A., Hik, D. S., Hofgaard, A., Jónsdóttir, I. S., Jorgenson, J., Klein, J., et al.: Plant functional trait change across a warming tundra biome, Nature, doi:10.1038/s41586-018-0563-7, 2018.

Bronaugh, D. and Werner, A.: zyp: Zhang + Yue-Pilon trends package, Pacific Climate Impacts Consortium. [online] Available from: https://CRAN.R-project.org/package=zyp, 2013.

Calmels, D., Gaillardet, J., Brenot, A. and France-Lanord, C.: Sustained sulfide oxidation by physical erosion processes in the Mackenzie River basin: Climatic perspectives, Geology, 35(11), 1003–1006, doi:10.1130/G24132A.1, 2007.

Campeau, A., Bishop, K., Nilsson, M. B., Klemedtsson, L., Laudon, H., Leith, F. I., Öquist, M. and Wallin, M. B.: Stable Carbon Isotopes Reveal Soil-Stream DIC Linkages in Contrasting Headwater Catchments, J. Geophys. Res. Biogeosci., 123(1), 149–167, doi:10.1002/2017JG004083, 2018.

Clark, I. D. and Fritz, P.: Environmental isotopes in hydrogeology, CRC Press/Lewis Publishers, Boca Raton, FL., 1997.

Crawford, J. T., Striegl, R. G., Wickland, K. P., Dornblaser, M. M. and Stanley, E. H.: Emissions of carbon dioxide and methane from a headwater stream network of interior Alaska, Journal of Geophysical Research: Biogeosciences, 118(2), 482–494, doi:10.1002/jgrg.20034, 2013.

Cray, H. A. and Pollard, W. H.: Vegetation Recovery Patterns Following Permafrost Disturbance in a Low Arctic Setting: Case Study of Herschel Island, Yukon, Canada, Arctic, Antarctic, and Alpine Research, 47(1), 99–113, doi:10.1657/AAAR0013-076, 2015.

Descolas-Gros, C. and Fontungne, M.: Stable carbon isotope fractionation by marine phytoplankton during photosynthesis, Plant, Cell and Environment, 13(3), 207–218, doi:10.1111/j.1365-3040.1990.tb01305.x, 1990.

Didan, K.: MOD13Q1 MODIS/Terra Vegetation Indices 16-Day L3 Global 250m SIN Grid V006 [Data set]., NASA EOSDIS LP DAAC, doi:doi: 10.5067/MODIS/MOD13Q1.006, 2015.

Doctor, D. H., Kendall, C., Sebestyen, S. D., Shanley, J. B., Ohte, N. and Boyer, E. W.: Carbon isotope fractionation of dissolved inorganic carbon (DIC) due to outgassing of carbon dioxide from a headwater stream, Hydrological Processes, 22(14), 2410–2423, doi:10.1002/hyp.6833, 2008.

Drake, T. W., Tank, S. E., Zhulidov, A. V., Holmes, R. M., Gurtovaya, T. and Spencer, R. G. M.: Increasing Alkalinity Export from Large Russian Arctic Rivers, Environmental Science & Technology, 52(15), 8302–8308, doi:10.1021/acs.est.8b01051, 2018a.

Drake, T. W., Guillemette, F., Hemingway, J. D., Chanton, J. P., Podgorski, D. C., Zimov, N. S. and Spencer, R. G. M.: The Ephemeral Signature of Permafrost Carbon in an Arctic Fluvial Network, Journal of Geophysical Research: Biogeosciences, 123, 1–11, doi:10.1029/2017JG004311, 2018b.

585   Duk-Rodkin, A. and Hughes, O. L.: Surficial geology, Fort McPherson-Bell River, Yukon-Northwest Territories, 1992.

Evans, J. S., Oakleaf, J., Cushman, S. A. and Theobald, D.: An ArcGIS Toolbox for Surface Gradient and Geomorphometric Modeling, version 2.0-0. [online] Available from: http://evansmurphy.wix.com/evansspatial (Accessed 2 December 2015), 2014.

590   Gaillardet, J., Dupré, B., Louvat, P. and Allegre, C. J.: Global silicate weathering and CO_2 consumption rates deduced from the chemistry of large rivers, Chemical Geology, 159(1), 3–30, doi:10.1016/S0009-2541(99)00031-5, 1999.

Gentsch, N., Mikutta, R., Shibistova, O., Wild, B., Schnecker, J., Richter, A., Urich, T., Gittel, A., Šantrůčková, H., Bárta, J., Lashchinskiy, N., Mueller, C. W., Fuß, R. and Guggenberger, G.: Properties and bioavailability of
595   particulate and mineral-associated organic matter in Arctic permafrost soils, Lower Kolyma Region, Russia, European Journal of Soil Science, 66(4), 722–734, doi:10.1111/ejss.12269, 2015.

Gordon, N. D., McMahon, T. A., Finlayson, B. L., Gippel, C. J. and Nathan, R. J., Eds.: Stream hydrology: an introduction for ecologists, 2nd ed., Wiley, Chichester, West Sussex, England ; Hoboken, N.J., 2004.

Hamilton, S. K. and Ostrom, N. E.: Measurement of the stable isotope ratio of dissolved N_2 in ^{15}N tracer
600   experiments, Limnology and Oceanography: Methods, 5(7), 233–240, 2007.

Hesslein, R. H., Rudd, J. W. M., Kelly, C., Ramlal, P. and Hallard, K. A.: Carbon dioxide pressure in surface waters of Canadian lakes, in Air-Water Mass Transfer: Selected Papers from the Second International Symposium on Gas Transfer at Water Surfaces, edited by S. C. Wilhelms and J. S. Gulliver, pp. 413–431, American Society of Civil Engineers, New York, New York., 1991.

605   Hilton, R. G. and West, A. J.: Mountains, erosion and the carbon cycle, Nat Rev Earth Environ, 1(6), 284–299, doi:10.1038/s43017-020-0058-6, 2020.

Hitchon, B. and Krouse, H. R.: Hydrogeochemistry of the surface waters of the Mackenzie River drainage basin, Canada-III. Stable isotopes of oxygen, carbon and sulphur, Geochimica et Cosmochimica Acta, 36, 1337–1357, 1972.

610   Horgby, Å., Boix Canadell, M., Ulseth, A. J., Vennemann, T. W. and Battin, T. J.: High-Resolution Spatial Sampling Identifies Groundwater as Driver of CO_2 Dynamics in an Alpine Stream Network, J. Geophys. Res. Biogeosci., 124(7), 1961–1976, doi:10.1029/2019JG005047, 2019.

Hornby, D. D.: RivEX (Version 10.25). [online] Available from: http://www.rivex.co.uk, 2017.

Hotchkiss, E. R., Hall Jr, R. O., Sponseller, R. A., Butman, D., Klaminder, J., Laudon, H., Rosvall, M. and Karlsson,
615   J.: Sources of and processes controlling CO_2 emissions change with the size of streams and rivers, Nature Geoscience, 8(9), 696–699, doi:10.1038/ngeo2507, 2015.

Huete, A., Didan, K., Miura, T., Rodriguez, E. P., Gao, X. and Ferreira, L. G.: Overview of the radiometric and biophysical performance of the MODIS vegetation indices, Remote Sensing of Environment, 83(1–2), 195–213, doi:10.1016/S0034-4257(02)00096-2, 2002.

620   Hutchins, R. H. S., Prairie, Y. T. and del Giorgio, P. A.: Large-Scale Landscape Drivers of CO_2, CH_4, DOC, and DIC in Boreal River Networks, Global Biogeochemical Cycles, 33(2), 125–142, doi:10.1029/2018GB006106, 2019.

Hutchins, R. H. S., Tank, S. E., Olefeldt, D., Quinton, W. L., Spence, C., Dion, N., Estop-Aragonés, C. and Mengistu, S. G.: Fluvial CO_2 and CH_4 patterns across wildfire-disturbed ecozones of subarctic Canada: Current status and implications for future change, Glob Change Biol, gcb.14960, doi:10.1111/gcb.14960, 2020.

625   Kendall, C., Doctor, D. H. and Young, M. B.: Environmental Isotope Applications in Hydrologic Studies, in Treatise on Geochemistry, vol. 7, edited by H. D. Holland and K. K. Turekian, pp. 273–327, Elsevier, Oxford., 2014.

Kokelj, S. V., Lacelle, D., Lantz, T. C., Tunnicliffe, J., Malone, L., Clark, I. D. and Chin, K. S.: Thawing of massive ground ice in mega slumps drives increases in stream sediment and solute flux across a range of watershed scales, 630   Journal of Geophysical Research: Earth Surface, 118(2), 681–692, doi:10.1002/jgrf.20063, 2013.

Kokelj, S. V., Tunnicliffe, J., Lacelle, D., Lantz, T. C., Chin, K. S. and Fraser, R.: Increased precipitation drives mega slump development and destabilization of ice-rich permafrost terrain, northwestern Canada, Global and Planetary Change, 129, 56–68, doi:10.1016/j.gloplacha.2015.02.008, 2015.

Kokelj, S. V., Lantz, T. C., Tunnicliffe, J., Segal, R. and Lacelle, R.: Climate-driven thaw of permafrost preserved 635   glacial landscapes, northwestern Canada, Geology, 45(4), 371–374, doi:10.1130/G38626.1, 2017a.

Kokelj, S. V., Tunnicliffe, J. F. and Lacelle, D.: The Peel Plateau of Northwestern Canada: An Ice-Rich Hummocky Moraine Landscape in Transition, in Landscapes and Landforms of Western Canada, edited by O. Slaymaker, pp. 109–122, Springer International Publishing, Cham., 2017b.

Kuznetsova, A., Brockhoff, P. B. and Christensen, R. H. B.: Package 'lmerTest.', 2018.

640   Lacelle, D., Fontaine, M., Pellerin, A., Kokelj, S. V. and Clark, I. D.: Legacy of Holocene Landscape Changes on Soil Biogeochemistry: A Perspective From Paleo-Active Layers in Northwestern Canada, J. Geophys. Res. Biogeosci., 2018JG004916, doi:10.1029/2018JG004916, 2019.

Lafrenière, M. J. and Sharp, M. J.: The Concentration and Fluorescence of Dissolved Organic Carbon (DOC) in Glacial and Nonglacial Catchments: Interpreting Hydrological Flow Routing and DOC Sources, Arctic, Antarctic, 645   and Alpine Research, 36(2), 156–165, 2004.

Lehn, G. O., Jacobson, A. D., Douglas, T. A., McClelland, J. W., Barker, A. J. and Khosh, M. S.: Constraining seasonal active layer dynamics and chemical weathering reactions occurring in North Slope Alaskan watersheds with major ion and isotope ($\delta^{34}S_{SO4}$, $\delta^{13}C_{DIC}$, $^{87}Sr/^{86}Sr$, $\delta^{44/40}Ca$, and $\delta^{44/42}Ca$) measurements, Geochimica et Cosmochimica Acta, 217, 399–420, doi:10.1016/j.gca.2017.07.042, 2017.

650   Levenstein, B., Culp, J. M. and Lento, J.: Sediment inputs from retrogressive thaw slumps drive algal biomass accumulation but not decomposition in Arctic streams, NWT, Freshwater Biology, doi:10.1111/fwb.13158, 2018.

Littlefair, C. A., Tank, S. E. and Kokelj, S. V.: Retrogressive thaw slumps temper dissolved organic carbon delivery to streams of the Peel Plateau, NWT, Canada, Biogeosciences, 14(23), 5487–5505, doi:10.5194/bg-14-5487-2017, 2017.

655   Lurry, D. L. and Kolbe, C. M.: Interagency Field Manual for the Collection of Water-Quality Data, USGS., 2000.

Malone, L., Lacelle, D., Kokelj, S. and Clark, I. D.: Impacts of hillslope thaw slumps on the geochemistry of permafrost catchments (Stony Creek watershed, NWT, Canada), Chemical Geology, 356, 38–49, doi:10.1016/j.chemgeo.2013.07.010, 2013.

Millero, F. J.: The thermodynamics of the carbonate system in seawater, Geochimica et Cosmochimica Acta, 43, 660   1651–1661, 1979.

Mook, W. G., Bommerson, J. C. and Staverman, W. H.: Carbon isotope fractionation between dissolved bicarbonate and gaseous carbon dioxide, Earth and Planetary Science Letters, 22(2), 169–176, 1974.

Norris, D. K.: Geology of the Northern Yukon and Northwestern District of Mackenzie, 1985.

Olefeldt, D., Goswami, S., Grosse, G., Hayes, D., Hugelius, G., Kuhry, P., McGuire, A. D., Romanovsky, V. E., Sannel, A. B. K., Schuur, E. A. G. and Turetsky, M. R.: Circumpolar distribution and carbon storage of thermokarst landscapes, Nature Communications, 7, 13043, doi:10.1038/ncomms13043, 2016.

Parkhurst, D. I. and Appelo, C. A. J.: Description of input and examples for PHREEQC version 3 – A computer program for speciation, batch- reaction, one-dimensional transport, and inverse geochemical calculations, vol. A43, p. 497, U.S. Geological Survey. [online] Available from: http://pubs.usgs.gov/tm/06/a43, 2013.

Pierrot, D., Lewis, E. and Wallace, D. W. R.: MS Excel program developed for CO_2 system calculations. [online] Available from: doi:10.3334/CDIAC/otg. CO2SYS_XLS_CDIAC105a, 2006.

Piper, A. M.: A graphic procedure in the geochemical interpretation of water-analyses, Transactions, American Geophysical Union, 25(6), 914, doi:10.1029/TR025i006p00914, 1944.

Poulin, B. A., Ryan, J. N. and Aiken, G. R.: Effects of Iron on Optical Properties of Dissolved Organic Matter, Environmental Science & Technology, 48(17), 10098–10106, doi:10.1021/es502670r, 2014.

R Core Team: R: A Language and Environment for Statistical Computing, R Foundation for Statistical Computing, Vienna, Austria. [online] Available from: http://www.r-project.org/, 2018.

Rawlins, M. A., Steele, M., Holland, M. M., Adam, J. C., Cherry, J. E., Francis, J. A., Groisman, P. Y., Hinzman, L. D., Huntington, T. G., Kane, D. L., Kimball, J. S., Kwok, R., Lammers, R. B., Lee, C. M., Lettenmaier, D. P., McDonald, K. C., Podest, E., Pundsack, J. W., Rudels, B., Serreze, M. C., Shiklomanov, A., Skagseth, Ø., Troy, T. J., Vörösmarty, C. J., Wensnahan, M., Wood, E. F., Woodgate, R., Yang, D., Zhang, K. and Zhang, T.: Analysis of the Arctic System for Freshwater Cycle Intensification: Observations and Expectations, Journal of Climate, 23(21), 5715–5737, doi:10.1175/2010JCLI3421.1, 2010.

Riley, S. J., DeGloria, S. D. and Elliot, R.: A terrain ruggedness index that quantifies topographic heterogeneity, Intermountain Journal of Sciences, 5(1–4), 23–27, 1999.

Sander, R.: Compilation of Henry's law constants (version 4.0) for water as solvent, Atmos. Chem. Phys., 15(8), 4399–4981, doi:10.5194/acp-15-4399-2015, 2015.

Schuur, E. A. G., McGuire, A. D., Schädel, C., Grosse, G., Harden, J. W., Hayes, D. J., Hugelius, G., Koven, C. D., Kuhry, P., Lawrence, D. M., Natali, S. M., Olefeldt, D., Romanovsky, V. E., Schaefer, K., Turetsky, M. R., Treat, C. C. and Vonk, J. E.: Climate change and the permafrost carbon feedback, Nature, 520(7546), 171–179, doi:10.1038/nature14338, 2015.

Segal, R. A., Lantz, T. C. and Kokelj, S. V.: Acceleration of thaw slump activity in glaciated landscapes of the Western Canadian Arctic, Environmental Research Letters, 11(3), 034025, doi:10.1088/1748-9326/11/3/034025, 2016.

Serreze, M. C. and Barry, R. G.: Processes and impacts of Arctic amplification: A research synthesis, Global and Planetary Change, 77(1–2), 85–96, doi:10.1016/j.gloplacha.2011.03.004, 2011.

Shakil, S., Tank, S. E., Kokelj, S. V., Vonk, J. E. and Zolkos, S.: Particulate dominance of organic carbon mobilization from thaw slumps on the Peel Plateau, NT: Quantification and implications for stream systems and permafrost carbon release, Environ. Res. Lett., doi:10.1088/1748-9326/abac36, 2020.

Sharp, M., Tranter, M., Brown, G. H. and Skidmore, M.: Rates of chemical denudation and CO_2 drawdown in a glacier-covered alpine catchment, Geology, 23(1), 61–64, 1995.

van der Sluijs, J., Kokelj, S. V., Fraser, R. H., Tunnicliffe, J. and Lacelle, D.: Permafrost Terrain Dynamics and Infrastructure Impacts Revealed by UAV Photogrammetry and Thermal Imaging, Remote Sensing, 30, 2018.

705   St. Pierre, K. A., St. Louis, V. L., Schiff, S. L., Lehnherr, I., Dainard, P. G., Gardner, A. S., Aukes, P. J. K. and Sharp, M. J.: Proglacial freshwaters are significant and previously unrecognized sinks of atmospheric CO_2, Proc Natl Acad Sci USA, 201904241, doi:10.1073/pnas.1904241116, 2019.

Stallard, R. F. and Edmond, J. M.: Geochemistry of the Amazon: 2. The Influence of Geology and Weathering Environment on the Dissolved Load, Journal of Geophysical Research, 88(C14), 9671–9688, 1983.

710   Striegl, R. G., Dornblaser, M. M., Aiken, G. R., Wickland, K. P. and Raymond, P. A.: Carbon export and cycling by the Yukon, Tanana, and Porcupine rivers, Alaska, 2001-2005, Water Resources Research, 43(2), doi:10.1029/2006WR005201, 2007.

Stubbins, A., Silva, L. M., Dittmar, T. and Van Stan, J. T.: Molecular and Optical Properties of Tree-Derived Dissolved Organic Matter in Throughfall and Stemflow from Live Oaks and Eastern Red Cedar, Frontiers in Earth Science, 5, doi:10.3389/feart.2017.00022, 2017.

715   Stumm, W. and Morgan, J. J.: Aquatic Chemistry: Chemical Equilibria and Rates in Natural Waters, 3rd ed., John Wiley & Son, Inc., New York., 1996.

Tank, S. E., Striegl, R. G., McClelland, J. W. and Kokelj, S. V.: Multi-decadal increases in dissolved organic carbon and alkalinity flux from the Mackenzie drainage basin to the Arctic Ocean, Environmental Research Letters, 11(5), 054015, doi:10.1088/1748-9326/11/5/054015, 2016.

720   Tank, S. E., Vonk, J. E., Walvoord, M. A., McClelland, J. W., Laurion, I. and Abbott, B. W.: Landscape matters: Predicting the biogeochemical effects of permafrost thaw on aquatic networks with a state factor approach, Permafrost and Periglac Process, ppp.2057, doi:10.1002/ppp.2057, 2020.

Toohey, R. C., Herman-Mercer, N. M., Schuster, P. F., Mutter, E. A. and Koch, J. C.: Multidecadal increases in the Yukon River Basin of chemical fluxes as indicators of changing flowpaths, groundwater, and permafrost,
725   Geophysical Research Letters, 43(23), 12,120-12,130, doi:10.1002/2016GL070817, 2016.

Torres, M. A., Moosdorf, N., Hartmann, J., Adkins, J. F. and West, A. J.: Glacial weathering, sulfide oxidation, and global carbon cycle feedbacks, Proceedings of the National Academy of Sciences, 114(33), 8716–8721, doi:10.1073/pnas.1702953114, 2017.

730   Turetsky, M. R., Abbott, B. W., Jones, M. C., Walter Anthony, K., Olefeldt, D., Schuur, E. A. G., Grosse, G., Kuhry, P., Hugelius, G., Koven, C., Lawrence, D. M., Gibson, C., Sannel, A. B. K. and McGuire, A. D.: Carbon release through abrupt permafrost thaw, Nature Geoscience, 13, 138–143, 2020.

Turner, J. V.: Kinetic fractionation of carbon-13 during calcium carbonate precipitation, Geochimica et Cosmochimica Acta, 46, 1183–1191, doi:10.1016/0016-7037(82)90004-7, 1982.

Vonk, J. E., Tank, S. E., Mann, P. J., Spencer, R. G. M., Treat, C. C., Striegl, R. G., Abbott, B. W. and Wickland, K.
735   P.: Biodegradability of dissolved organic carbon in permafrost soils and aquatic systems: a meta-analysis, Biogeosciences, 12(23), 6915–6930, doi:10.5194/bg-12-6915-2015, 2015.

Vonk, J. E., Tank, S. E. and Walvoord, M. A.: Integrating hydrology and biogeochemistry across frozen landscapes, Nat Commun, 10(1), 5377, doi:10.1038/s41467-019-13361-5, 2019.

Wadham, J. L., Hawkings, J. R., Tarasov, L., Gregoire, L. J., Spencer, R. G. M., Gutjahr, M., Ridgwell, A. and
740   Kohfeld, K. E.: Ice sheets matter for the global carbon cycle, Nat Commun, 10(1), 3567, doi:10.1038/s41467-019-11394-4, 2019.

Walvoord, M. A. and Kurylyk, B. L.: Hydrologic Impacts of Thawing Permafrost—A Review, Vadose Zone Journal, 15(6), 0, doi:10.2136/vzj2016.01.0010, 2016.

745 Weishaar, J. L., Aiken, G. R., Bergamaschi, B. A., Fram, M. S., Fujii, R. and Mopper, K.: Evaluation of Specific Ultraviolet Absorbance as an Indicator of the Chemical Composition and Reactivity of Dissolved Organic Carbon, Environmental Science & Technology, 37(20), 4702–4708, doi:10.1021/es030360x, 2003.

Weiss, R. F.: Carbon dioxide in water and seawater: the solubility of a non-ideal gas, Marine Chemistry, 2(3), 203–215, 1974.

750 Wiesenburg, D. A. and Guinasso, N. L.: Equilibrium solubilities of methane, carbon monoxide, and hydrogen in water and sea water, Journal of Chemical and Engineering Data, 24(4), 356–360, 1979.

Yue, S., Pilon, P., Phinney, B. and Cavadias, G.: The influence of autocorrelation on the ability to detect trend in hydrological series, Hydrological Processes, 16(9), 1807–1829, doi:10.1002/hyp.1095, 2002.

Zhang, J., Quay, P. D. and Wilbur, D. O.: Carbon isotope fractionation during gas-water exchange and dissolution of CO_2, Geochimica et Cosmochimica Acta, 59(1), 107–114, 1995.

755 Zolkos, S. and Tank, S. E.: Experimental Evidence That Permafrost Thaw History and Mineral Composition Shape Abiotic Carbon Cycling in Thermokarst-Affected Stream Networks, Front. Earth Sci., 8(152), 17, doi:10.3389/feart.2020.00152, 2020.

Zolkos, S., Tank, S. E. and Kokelj, S. V.: Mineral Weathering and the Permafrost Carbon-Climate Feedback, Geophysical Research Letters, doi:10.1029/2018GL078748, 2018.

760 Zolkos, S., Tank, S. E., Striegl, R. G. and Kokelj, S. V.: Thermokarst Effects on Carbon Dioxide and Methane Fluxes in Streams on the Peel Plateau (NWT, Canada), J. Geophys. Res. Biogeosci., 124(7), 1781–1798, doi:10.1029/2019JG005038, 2019.

Zuur, A. F., Ed.: Mixed effects models and extensions in ecology with R, Springer, New York, NY., 2009.

Zuur, A. F., Ieno, E. N. and Elphick, C. S.: A protocol for data exploration to avoid common statistical problems, 765 Methods in Ecology and Evolution, 1(1), 3–14, doi:10.1111/j.2041-210X.2009.00001.x, 2010.

767 **Table 1.** Mineral weathering equations used to create Piper diagram end-members. H_2CO_3 = carbonic acid, H_2SO_4 =
768 sulfuric acid. H_2CO_3 includes dissolved $CO_{2(g)}$.

Eq.	Reaction	Equation	Reference
1	H_2CO_3 carbonate weathering (CACW)	$H_2CO_3 + (Ca,Mg)CO_3 \rightarrow (Ca^{2+},Mg^{2+}) + 2HCO_3^-$	Lehn et al. (2017)
2	H_2CO_3 silicate weathering (CASW)	$2H_2CO_3 + 3H_2O + (Ca,Mg)Al_2Si_2O_8 \rightarrow (Ca^{2+},Mg^{2+}) + 2HCO_3^- + 2Al_2Si_2O_5(OH)_4$	Lehn et al. (2017)
3	H_2SO_4 carbonate weathering (SACW)	$H_2SO_4 + 2(Ca,Mg)CO_3 \rightarrow 2(Ca^{2+},Mg^{2+}) + SO_4^{2-} + 2HCO_3^-$	Lehn et al. (2017)
4	H_2SO_4 silicate weathering (SASW)	$H_2SO_4 + H_2O + (Ca,Mg)Al_2Si_2O_8 \rightarrow (Ca^{2+},Mg^{2+}) + SO_4^{2-} + Al_2Si_2O_5(OH)_4$	Lehn et al. (2017)
5	Sulfate salt dissolution (SSD)	$(Ca,Mg)SO_4 \rightarrow (Ca^{2+},Mg^{2+}) + SO_4^{2-}$	Lehn et al. (2017)
6	Sulfide oxidation	$FeS_2 + 15/4 O_2 + 7/2 H_2O \rightarrow Fe(OH_3) + 2H^+ + SO_4^{2-}$	Calmels et al. (2007)
7	Carbonate weathering by H_2SO_4 in excess ($SA_{ex}CW$)	$2H_2SO_4 + CaMg(CO_3)_2 \rightarrow Ca^{2+} + Mg^{2+} + 2SO_4^{2-} + 2H_2CO_3$	Stallard and Edmond (1983)
8	Carbonate equilibrium / DIC speciation	$H_2O + CO_{2(g)} \rightleftharpoons H_2CO_3 \rightleftharpoons H^+ + HCO_3^- \rightleftharpoons 2H^+ + CO_3^{2-}$	Stumm and Morgan (1996)

769

770 **Table 2.** Geochemistry of mainstem and tributary sites along Dempster and Stony Creeks. Retrogressive thaw slump
771 (RTS) FM2 runoff samples collected on July 31, 2017, except where noted ([†]July 30, 2017). RTS FM2 runoff site #5
772 was nearest the confluence with Dempster Creek (Fig. 1). Area = watershed area, SE = standard error. *Not RTS-
773 affected.

Type	Site	pH	Cond ($\mu S\ cm^{-1}$)	pCO_2 (μatm)	CO_2 (μM)	HCO_3^- (μM)	CO_3^{2-} (μM)	DIC (uM)	δ^{13}C-DIC (‰VPDB)	δ^{13}C-CO_2 (‰VPDB)	DOC (μM)	$SUVA_{254}$ (L mgC^{-1} m^{-1})	TSS (mg L^{-1})	Area (km²)	RTS (% area)
RTS FM2 (Runoff)	1	7.72	1370	1046	43	1510	5.2	1559	–	-12.1	758	1.85	–	–	–
	2	7.51	1816	1534	60	1439	3.5	1502	–	-11.4	–	–	–	–	–
	3	7.71	1920	914	37	1419	5.4	1462	–	-10.3	–	–	–	–	–
	4	7.73	1903	878	38	1391	5.1	1433	–	-10.0	–	–	–	–	–
	5	7.80	1986	742	33	1386	5.8	1424	–	-11.2	–	–	–	–	–
	5[†]	7.82	1653	691	29	1450	7.1	1487	-1.0	-11.6	726	1.84	15805	–	–
	Mean	7.69	1799	1023	42	1429	5.01	1476		-11.0	758	1.85			
	(SE)	(0.05)	(111)	(137)	(5)	(23)	(0.39)	(25)	–	(0.4)	(152)	(0.37)	–	–	–
Dempster (Mainstem)	1*	5.82	52	2467	124	115	0.0	239	-15.0	-21.6	960	3.66	5	2	0.00
	2	7.55	958	686	35	1321	4.8	1361	-4.2	-16.0	790	2.53	11795	16	3.18
	3	7.54	655	656	31	1073	3.6	1107	-5.3	-15.6	823	2.93	9165	24	2.18
	4	7.35	416	600	30	946	2.9	978	-5.7	-18.5	1156	3.28	2797	57	1.19
	Mean	7.07	520	1102	55	864	2.8	921	-7.5	-17.9	933	3.10	5940	25	1.64
	(SE)	(0.42)	(191)	(455)	(23)	(261)	(1.0)	(241)	(2.5)	(1.4)	(83)	(0.24)	(2735)	(12)	(0.68)
Dempster (Tributary)	2*	7.56	390	836	50	1233	2.8	1286	-10.5	-21.3	1053	3.46	26	2	0.00
	3	7.32	171	478	23	561	1.3	586	-7.2	-18.1	1241	3.65	985	11	1.47
	4	7.30	236	552	27	697	1.7	726	-8.0	-16.5	922	3.61	223	168	0.40
	Mean	7.39	266	622	34	830	1.9	866	-8.6	-18.7	1072	3.57	411	61	0.62
	(SE)	(0.08)	(65)	(109)	(8)	(205)	(0.4)	(214)	(1.0)	(1.4)	(93)	(0.06)	(292)	(54)	(0.44)
Stony (Mainstem)	1*	5.66	406	543	33	33	0.0	65	-11.6	-13.8	102	1.29	3	83	0.00
	2	6.37	396	448	25	69	0.0	94	-8.0	-15.1	124	1.58	920	136	0.01
	3	7.01	334	473	27	112	0.0	139	-6.9	-15.3	202	2.16	799	176	0.27
	4	6.69	283	444	25	248	0.2	273	-8.9	-17.6	306	2.77	462	479	0.39
	5	7.20	279	482	27	325	0.4	353	-8.4	-17.6	364	3.09	507	490	0.38
	6	7.33	290	461	25	382	0.5	408	-7.8	-18.1	385	3.01	665	626	0.33
	7	7.30	293	461	25	409	0.6	435	-8.1	-18.1	390	2.99	761	689	0.32
	8	7.30	279	519	27	461	0.7	489	-7.8	-18.1	551	3.19	1073	995	0.36
	Mean	6.86	320	479	27	255	0.3	282	-8.4	-16.7	303	2.51	649	459	0.26
	(SE)	(0.21)	(19)	(12)	(1)	(59)	(0.1)	(58)	(0.5)	(0.6)	(54)	(0.26)	(117)	(111)	(0.06)
Stony (Tributary)	1*	5.00	524	451	25	1	0.0	26	-15.6	-12.3	101	0.73	5	26	0.00
	2	6.71	226	501	28	449	0.7	478	-5.0	-15.9	437	2.22	39568	7	3.50
	3	7.11	148	448	26	338	0.4	365	-9.3	-18.0	458	3.12	10	59	0.16
	4	6.53	245	572	32	375	0.4	407	-8.5	-19.4	550	3.31	704	194	0.67
	5	7.00	479	494	26	601	1.3	628	-7.0	-18.0	596	2.88	1270	104	0.13
	6	7.37	260	498	27	633	1.4	661	-8.0	-18.3	1142	3.34	1936	38	0.20
	7	7.32	230	475	26	570	1.2	597	-10.7	-18.0	1078	3.56	1258	227	0.60
	Mean	6.72	302	491	27	424	0.8	452	-9.1	-17.1	623	2.74	6393	94	0.75
	(SE)	(0.31)	(53)	(16)	(1)	(82)	(0.2)	(83)	(1.3)	(0.9)	(140)	(0.37)	(5536)	(32)	(0.47)

774

775 **Table 3.** Characteristics of Stony Creek tributary watersheds (upper panel) and results from the multiple linear
776 regression model (lower panel). The Stony Creek watershed contained 109 retrogressive thaw slumps (RTS), 92 of
777 which were in the major tributaries of the Stony Creek mainstem. TR = terrain roughness. EVI = enhanced
778 vegetation index. Values were used in the multiple linear regression model to determine the drivers of HCO_3^- yields
779 in Stony Creek tributary watersheds. Model results are shown in the lower panel. Covariates eliminated during
780 model selection (RTS_n, TR, EVI) are not reflected in the lower panel or final model: $ln$$HCO_3^-$ yield = 1.04lnWater
781 yield + 0.35$ln$$RTS_{area}$ + 8.76.

Tributary	HCO_3^- yield ($\mu M\ m^{-2}\ d^{-1}$)	Water yield ($cm\ d^{-1}$)	RTS (% area)	RTS (n)	Mean TR (m)	Mean EVI
1	2	0.20	0.00	0	16.2	0.28
2	2819	0.61	3.50	6	3.4	0.48
3	1047	0.18	0.16	3	6.7	0.45
4	227	0.04	0.67	50	4.5	0.45
5	1378	0.12	0.31	11	4.7	0.46
6	3056	0.28	0.20	8	2.7	0.47
7	821	0.07	0.60	14	3.6	0.45

Covariate	Estimate	t	p
lnWater yield	1.04	3.6	0.02
$ln$$RTS_{area}$	0.35	10.5	< 0.001

782
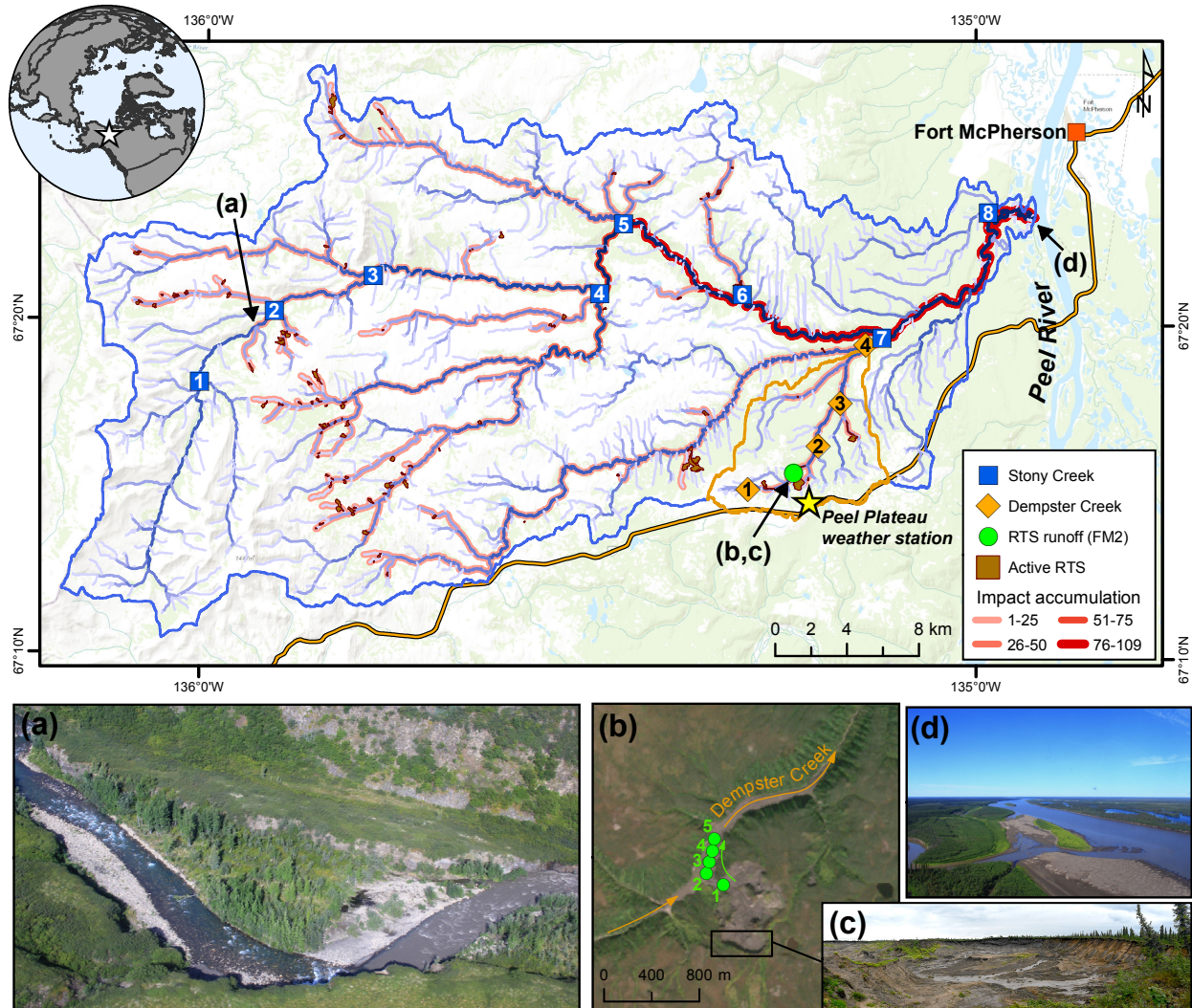
Figure 1. Sampling sites on the Peel Plateau (NWT, Canada). Water samples were collected along the mainstem Dempster and Stony Creeks ($n = 12$) and major tributaries ($n = 10$), and from the rill runoff at retrogressive thaw slump (RTS) FM2. Numbers within symbols are sampling sites (Tables 1 and A1). RTS impact accumulation represents the number of active RTSs affecting upstream reaches ($n = 109$) (see Methods Sect. 2.6). (a) Aerial photograph of Stony Creek where it was first impacted by RTS activity. (b) RTS FM2 runoff transect sampling scheme. RTS FM2 spans ~40 ha, its headwall (c) reaches ~25 m in height, and the debris tongue contains 2×10^6 m^3 of sediment (van der Sluijs et al., 2018). (d) Aerial photograph of the Stony Creek (lower left) flowing into the Peel River. Satellite image of RTS FM2 in September 2017 (b) obtained from Copernicus Sentinel data (European Space Agency, https://sentinel.esa.int/). Basemap: Esri ArcGIS Online © OpenStreetMap contributors, GIS User Community.
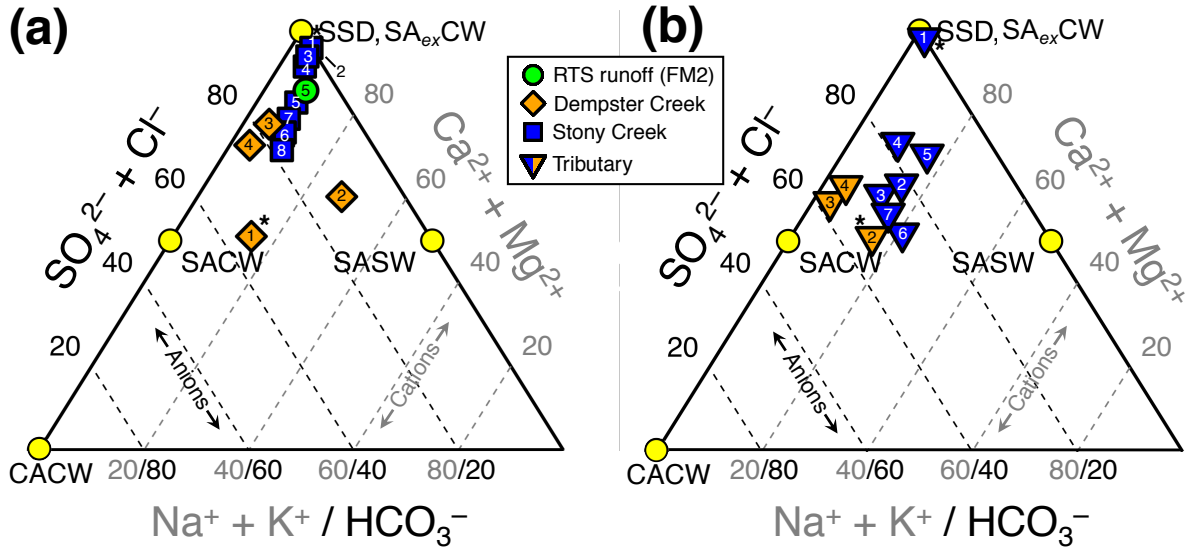
795
796 **Figure 2.** Piper diagrams (modified to show the upper half of the diamond plot) showing stream chemistry of the (**a**)
797 mainstem sites and (**b**) tributary and retrogressive thaw slump (RTS) FM2 runoff sites. Axes and corresponding text
798 in gray and black reflect the proportions of cations and anions, respectively. Mineral weathering end-members were
799 derived from the proportional concentration (meq L^{-1}) of solutes generated by H_2CO_3 carbonate weathering (CACW,
800 Eq. 1), H_2SO_4 carbonate weathering (SACW, Eq. 3), H_2SO_4 silicate weathering (SASW, Eq. 4), sulfate salt (e.g.
801 gypsum) dissolution (SSD, Eq. 5), and carbonate weathering by H_2SO_4 in excess (SA$_{ex}$CW, Eq. 7). Site numbers
802 given within symbols (Table A1). ***Site was not affected by RTSs.
803
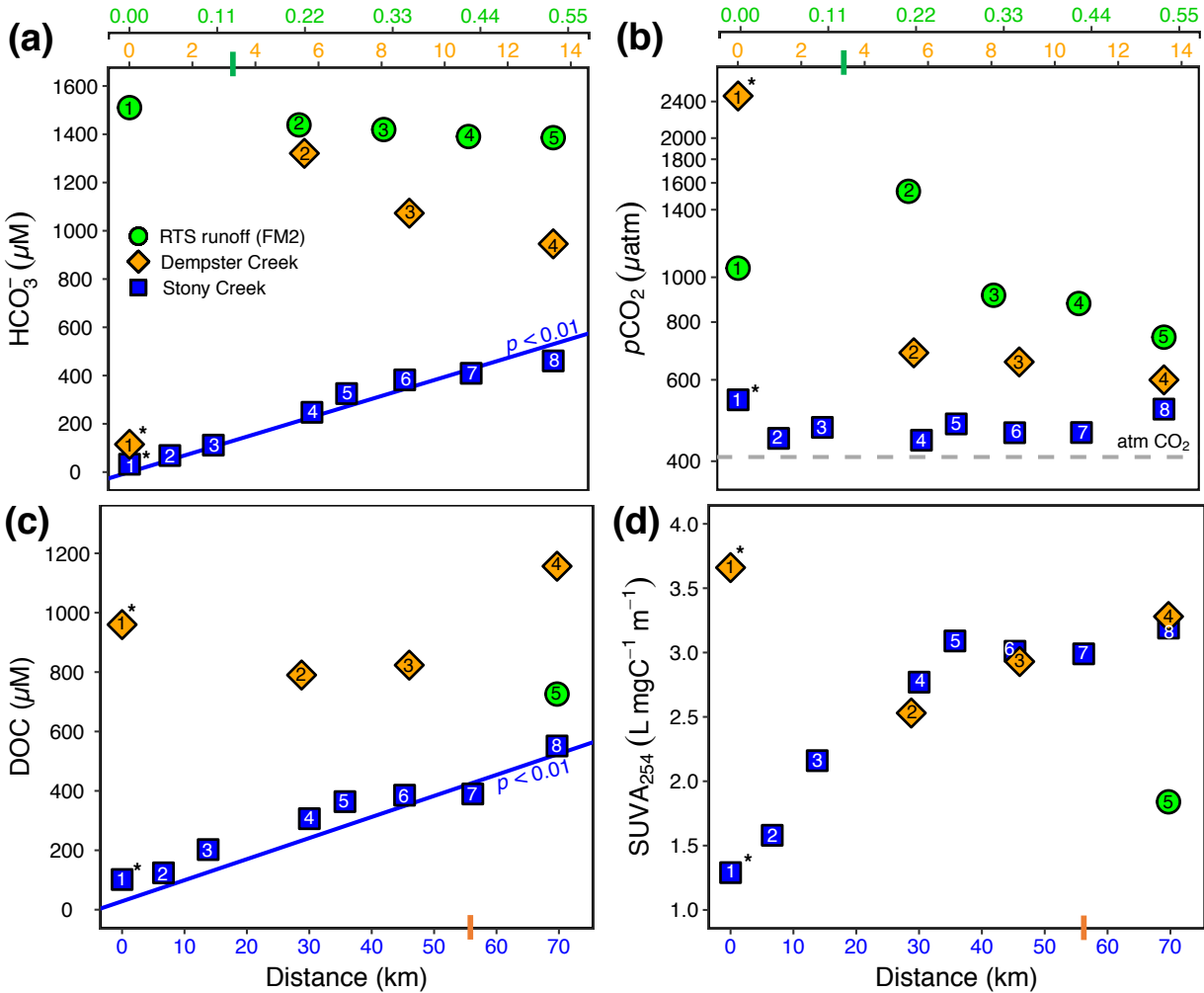
804
805 **Figure 3.** (**a**) HCO_3^-, (**b**) pCO_2, (**c**) dissolved organic carbon (DOC), and (**d**) $SUVA_{254}$ along the RTS FM2 runoff
806 transect and the mainstem Stony and Dempster Creeks (see locations in Fig. 1). For the RTS FM2 runoff, DOC and
807 $SUVA_{254}$ were sampled only at 0.55 km. Note different x-axis scales for the FM2 runoff transect (0–0.55 km, upper
808 x-axis), Dempster Creek (0–14 km, below RTS FM2 x-axis) and Stony Creek (0–70 km, lower x-axis). Regression
809 lines in (**a**) and (**c**) are from a Mann-Kendall test (details in Sect. 2.7). Bars on x-axes indicate where RTS FM2
810 runoff enters the Dempster Creek transect (3.3 km) and where Dempster Creek enters Stony Creek (56 km). Site
811 numbers are given within symbols (Table A1). *****Site was not affected by RTSs.
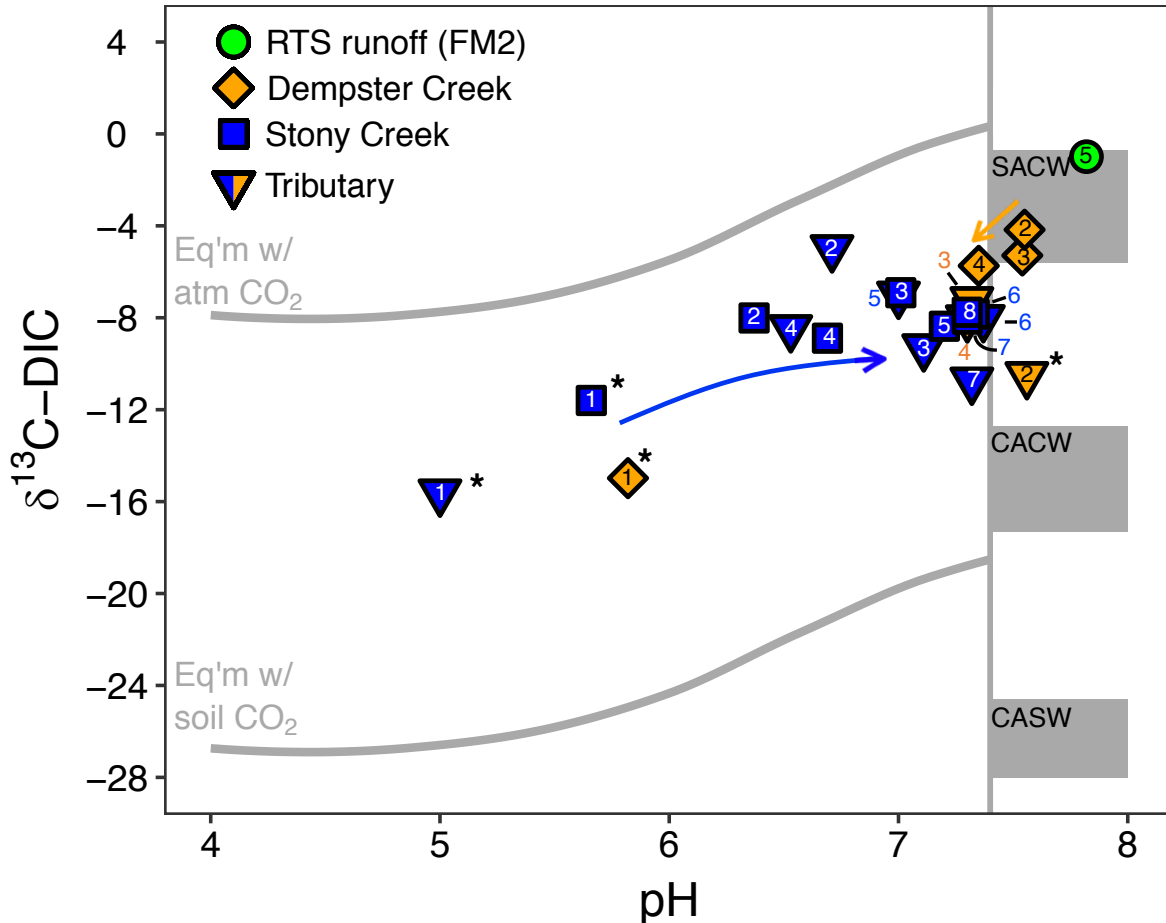
812
Figure 4. The pH and composition of dissolved inorganic carbon stable isotopes (δ^{13}C-DIC) in streams. The upper
814 and lower reference lines depict theoretical end-members for equilibrium reactions (mixing with atmospheric and
815 biotic CO_2, respectively). Gray boxes span theoretical end-member values for kinetically controlled mineral
816 weathering reactions (SACW = H_2SO_4 carbonate weathering, CACW = H_2CO_3 carbonate weathering, CASW =
817 H_2CO_3 silicate weathering) (see Sect. 2.4 for derivation of end-members). The vertical line corresponds to the pH at
818 which $\geq$ 90% of DIC is HCO_3^-, for the mean observed stream water temperature (11.7°C). At pH < 7.4, δ^{13}C-DIC
819 values primarily reflect equilibrium (rather than kinetic) controls on DIC cycling. Arrows reflect increasing
820 downstream distance from the headwaters in Stony Creek and from the first retrogressive thaw slump (RTS)
821 affected site in Dempster Creek. Site numbers given within symbols (Table A1). *****Site was not affected by RTSs.
822
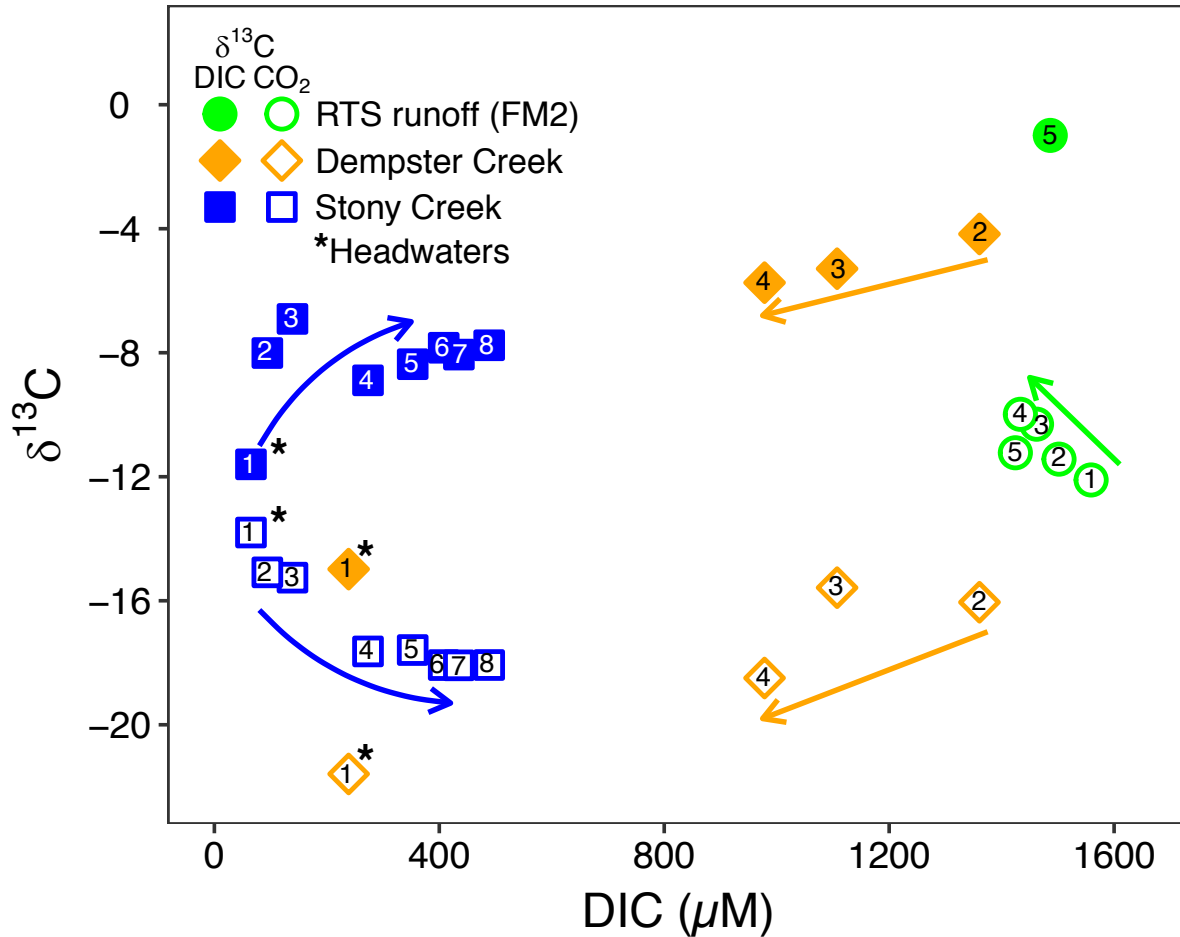
823
824 **Figure 5.** The composition of DIC and CO_2 stable isotopes at varying DIC concentrations along the Dempster and
825 Stony Creek mainstems, and in the rill runoff of retrogressive thaw slump (RTS) FM2. Arrows reflect increasing
826 downstream distance from headwaters in Stony Creek, from the first RTS-affected site in Dempster Creek, and from
827 the start of the FM2 runoff transect. Site numbers given within symbols (Table A1). ***Site in headwaters and not
828 affected by RTSs.
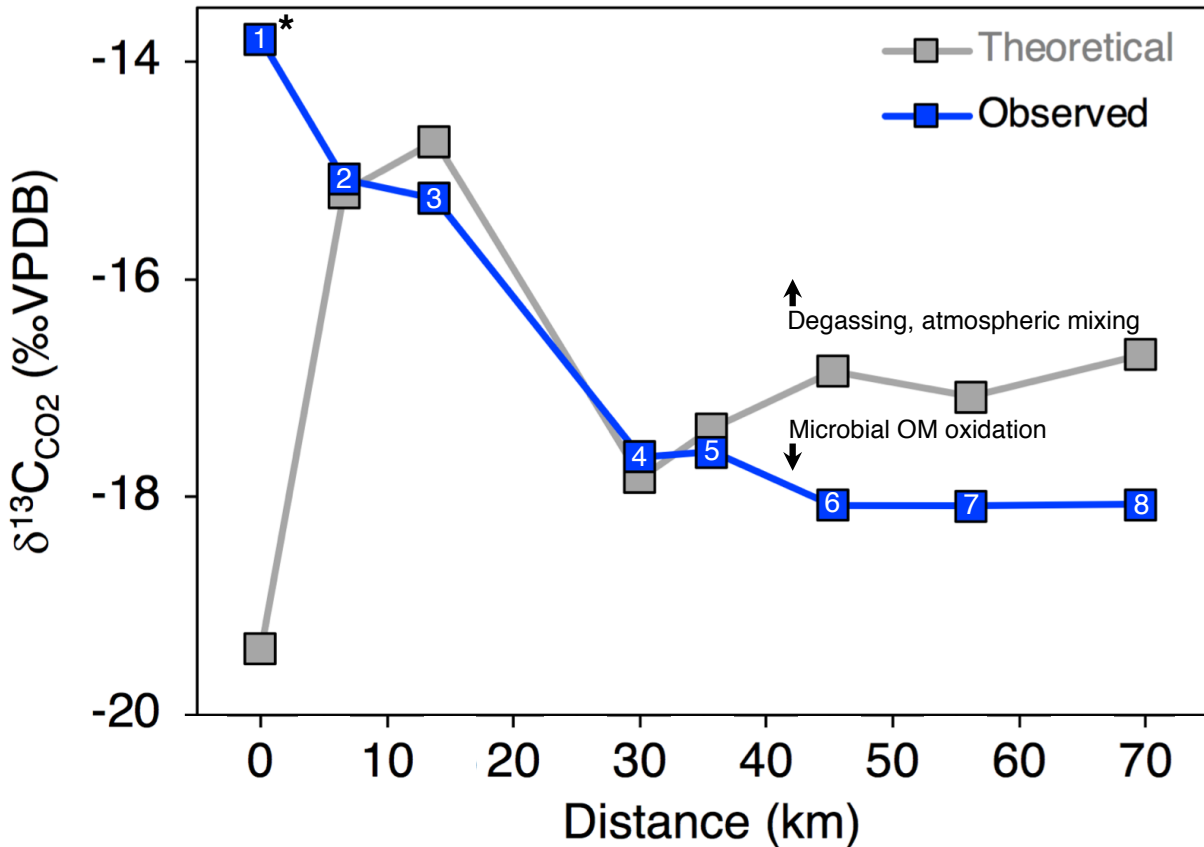
829
Figure 6. Observed and expected δ^{13}C-CO$_2$ values along the Stony Creek mainstem. Theoretical δ^{13}C-CO$_2$ values
were calculated as detailed in Sect. 2.6 and reflect changes in CO$_2$ due to DIC speciation (i.e. H$_2$CO$_3$ $\rightleftharpoons$ H$^+$ + HCO$_3^-$,
Eq. 8). Deviation from theoretical δ^{13}C-CO$_2$ values by observed values thus indicates isotopic effects from
degassing and/or microbial oxidation of organic matter (OM), as indicated by the arrows. Site numbers given within
symbols (Table A1). ***Site was not affected by retrogressive thaw slumps.
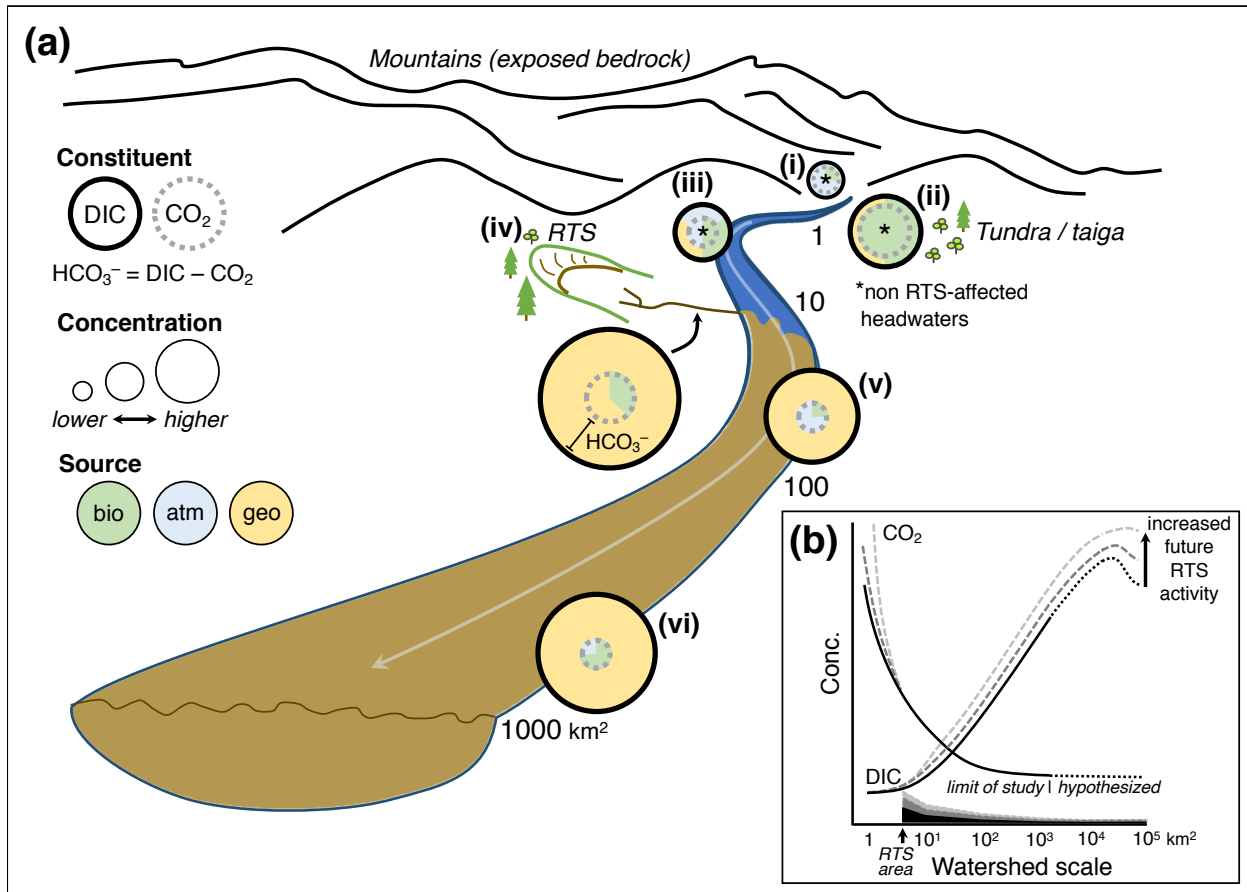
Figure 7. (**a**) Conceptual model of retrogressive thaw slump (RTS) activity and mineral weathering effects on carbon cycling in glaciated thermokarst terrains like the Peel Plateau. Source abbreviations: bio = biogenic, atm = atmospheric, geo = geogenic. (**b**) RTS effects on CO_2 and DIC ($\Sigma[CO_2$, carbonate alkalinity]) observed in this study (dark solid line), projected across broader scales in the modern-day (dark dotted line), and under hypothetical future scenarios of increasing RTS activity (medium- and light-gray dashed lines). Shaded regions along x-axis depict relative RTS area approximated for modern-day (black) and for hypothetical future increases in RTS area (medium- and light-gray).

Appendices

844 **Table A1.** Sampling site characteristics. Retrogressive thaw slump (RTS) FM2 runoff was a tributary to Dempster
845 Creek (confluence upstream of site 2) and Dempster Creek was a tributary to Stony Creek (confluence upstream of
846 site 8). Coordinates reported in decimal degrees. ***Site was not affected by RTSs.**

Creek	Site	Type	Latitude (DD)	Longitude (DD)	Sampling date	Distance (km)	Elevation (m)	Stream order (Strahler)
RTS FM2	1	Runoff	67.25639	-135.23422	7/31/17	0	–	1
RTS FM2	2	Runoff	67.25726	-135.23756	7/31/17	0.22	–	1
RTS FM2	3	Runoff	67.25813	-135.23700	7/31/17	0.33	–	1
RTS FM2	4	Runoff	67.25894	-135.23636	7/31/17	0.44	–	1
RTS FM2	5	Runoff	67.25986	-135.23595	7/31/17	0.55	–	1
RTS FM2	5	Runoff	67.25981	-135.23587	7/30/17	–	271	1
Dempster	1*	Mainstem	67.25181	-135.29456	7/31/17	0	407	3
Dempster	2	Mainstem	67.27364	-135.20409	7/29/17	5.6	194	4
Dempster	3	Mainstem	67.29500	-135.17570	7/27/17	8.9	132	4
Dempster	4	Mainstem	67.32336	-135.14133	7/27/17	13.5	67	4
Dempster	2*	Tributary	67.27364	-135.20367	7/29/17	–	–	2
Dempster	3	Tributary	67.29497	-135.17538	7/27/17	–	–	3
Dempster	4	Tributary	67.32414	-135.14252	7/27/17	–	–	4
Stony	1*	Mainstem	67.30280	-136.00468	7/27/17	0	575	4
Stony	2	Mainstem	67.33878	-135.90912	7/27/17	6.6	474	4
Stony	3	Mainstem	67.35704	-135.78165	7/25/17	13.8	382	4
Stony	4	Mainstem	67.34913	-135.48802	7/25/17	30.0	230	5
Stony	5	Mainstem	67.38380	-135.45747	7/25/17	35.7	184	6
Stony	6	Mainstem	67.34879	-135.30302	7/25/17	45.3	123	6
Stony	7	Mainstem	67.32732	-135.12160	7/25/17	56.2	57	6
Stony	8	Mainstem	67.39000	-134.98380	7/25/17	69.7	6	6
Stony	1*	Tributary	67.30367	-136.00421	7/27/17	–	–	3
Stony	2	Tributary	67.33933	-135.90836	7/27/17	–	–	3
Stony	3	Tributary	67.35719	-135.78311	7/25/17	–	–	4
Stony	4	Tributary	67.34860	-135.48773	7/25/17	–	–	5
Stony	5	Tributary	67.38467	-135.45607	7/25/17	–	–	4
Stony	6	Tributary	67.34882	-135.30196	7/25/17	–	–	4
Stony	7	Tributary	67.32703	-135.12213	7/25/17	–	–	5

847
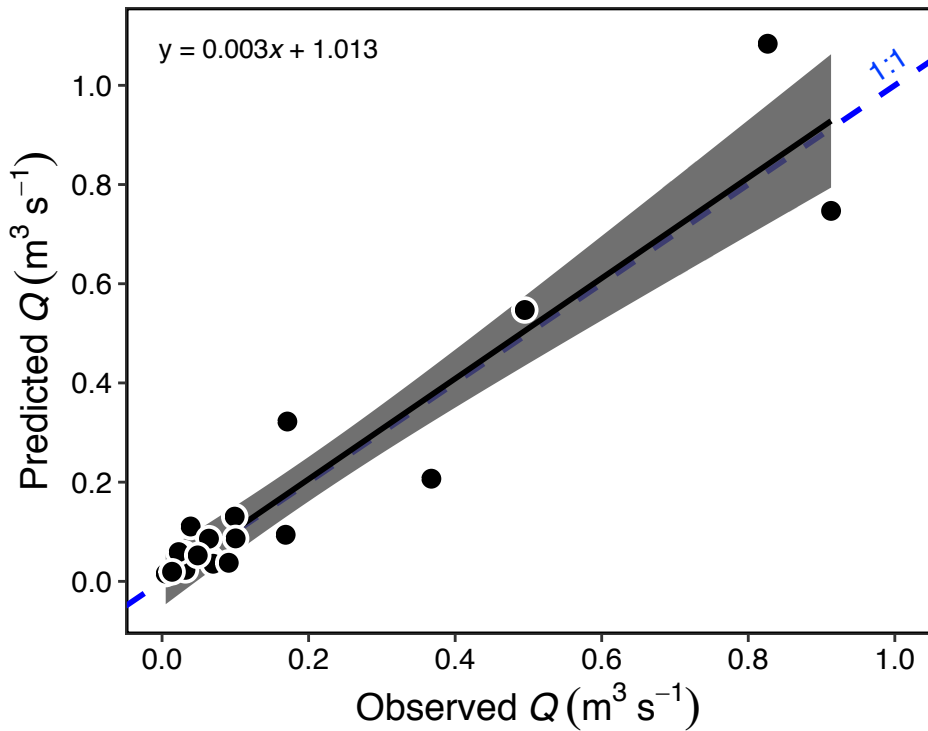
848
849 **Figure A1.** Estimated vs. measured discharge (Q) ($p < 0.001$, $R^2 = 0.89$, $F_{1,18} = 150$) for 20 streams in the Stony
850 Creek watershed. Grey band represents the 95% confidence interval shown around the regression. Estimates were
851 made using measurements of stream width, Q, and a hydraulic geometry model (Gordon et al., 2004) (see Sect. 2.6).
852 The model (Eq. 1) was used to estimate Q in the Stony Creek tributaries.
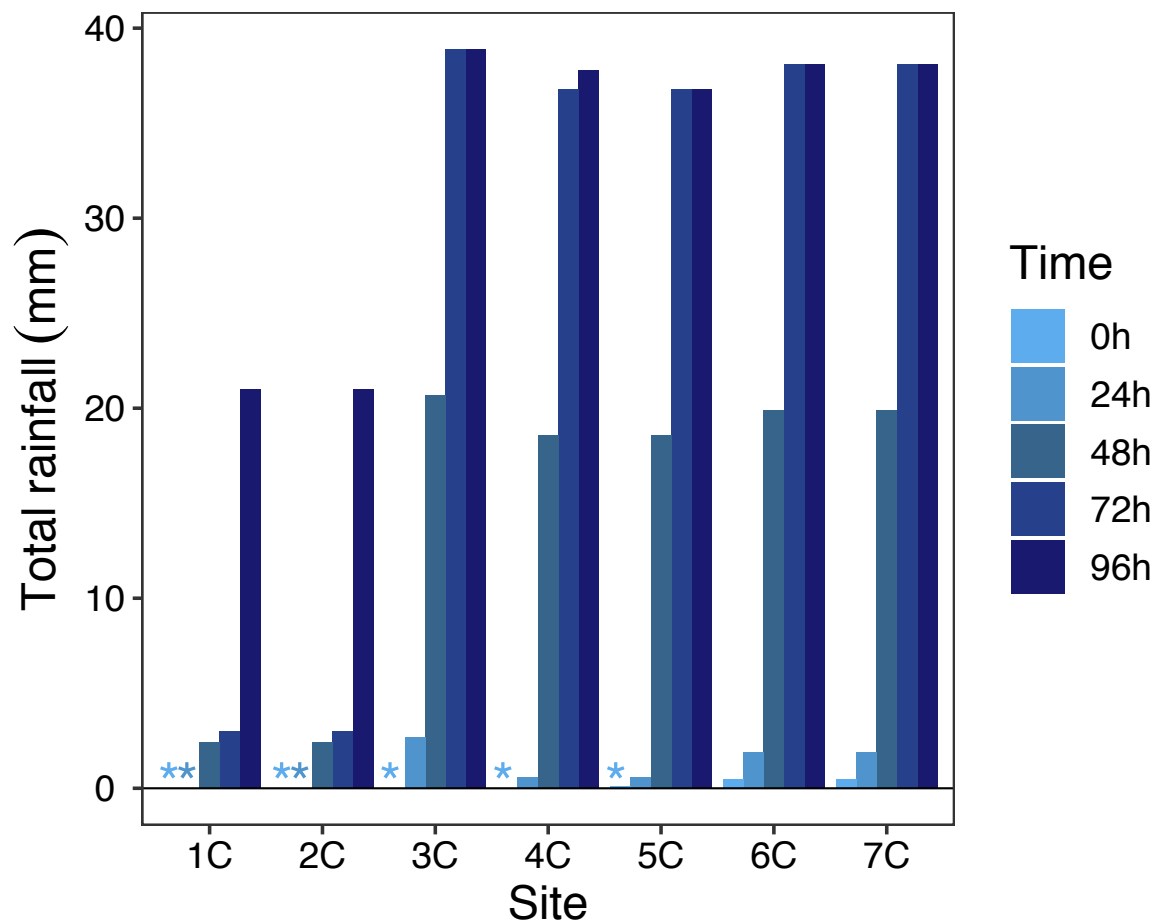
853
854   **Figure A2.** Total rainfall in 24 h increments preceding the sampling of each Stony Creek tributary. Rainfall data
855   were obtained from a Government of Northwest Territories weather station on the Peel Plateau located near the RTS
856   FM2. Locations of tributary sampling sites and the weather station are shown in Fig. 1. *Indicates no rainfall in the
857   24 h window.